La investigación reportada en esta tesis es parte de los programas de investigación del CICESE (Centro de Investigación Científica y de Educación Superior de Ensenada, B.C.).

La investigación fue financiada por el CONACYT (Consejo Nacional de Ciencia y Tecnología).

Centro de Investigación Científica y de Educación Superior de Ensenada, Baja California

Maestría en Ciencias en Nanociencias

First principles studies applied to Mn-Ga alloys: magnetism and surface reconstructions

Tesis

para cubrir parcialmente los requisitos necesarios para obtener el grado de

Maestro en Ciencias

Presenta:

Ricardo Miguel Ruvalcaba Briones

Ensenada, Baja California, México

2022

Tesis defendida por

Ricardo Miguel Ruvalcaba Briones

y aprobada por el siguiente Comité

Dr. Jonathan Guerrero Sánchez
Director de tesis

Dr. Hugo Alejandro Borbón Núñez

Dr. Luis Alonso Gallardo Delgado

Dr. José Manuel Romo Herrera
Coordinador del Posgrado en Nanociencias

Dr. Pedro Negrete Regagnon
Director de Estudios de Posgrado

Abstract of the thesis presented by Ricardo Miguel Ruvalcaba Briones as a partial requirement to obtain the Master of Science degree in Nanosciences.

First principles studies applied to Mn-Ga alloys: magnetism and surface reconstructions

Abstract approved by:

Dr. Jonathan Guerrero Sánchez
Thesis Director

This thesis presents the results of an extensive set of first-principles calculations via Density Functional Theory to characterize the structural, electronic, and magnetic properties of the bulk and (001) surface structures of three Mn-Ga alloys: α-Mn, D0_{22}-Mn_3Ga, and L1_0-MnGa. Their bulk properties were characterized, and their most stable surface reconstructions were determined. The first-ever theoretical models for the complex α-Mn surfaces are proposed, and the behavior of the magnetic moments at the most stable surface is discussed. Experimental and theoretical STM images of the row- and square-reconstructions are compared and are found in excellent agreement. Also, the role of C diffusion on the magnetic enhancement of D0_{22}-Mn_3Ga surfaces was examined. It is discussed in terms of the surface effect, the magnetoelastic effect, the superexchange interaction, and the Density of States of each atom. Finally, two 1×2 Ga-terminated surface reconstructions of L1_0-MnGa were studied. Their magnetic properties are discussed in terms of the surface effect, the Densities of States of each atom, and magnetization density. It was determined that the Cu-substituted reconstruction could behave like a magnetic Single-Atom Alloy Catalyst.

Keywords: Density Functional Theory, surface reconstructions, electronic structure, magnetic anisotropy

Resumen de la tesis que presenta Ricardo Miguel Ruvalcaba Briones como requisito parcial para la obtención del grado de Maestro en Ciencias en Nanociencias.

Estudios de primeros principios aplicados a aleaciones de Mn-Ga: magnetismo y reconstrucciones superficiales

Resumen aprobado por:

Dr. Jonathan Guerrero Sánchez
Director de tesis

En esta tesis se presentan los resultados de un gran conjunto de cálculos de primeros principios a través de la Teoría del Funcional de la Densidad para caracterizar las propiedades estructurales, electrónicas y magnéticas de los bultos y las superficies (001) de tres aleaciones de Mn-Ga: α-Mn, D0_{22}-Mn_3Ga y L1_0-MnGa. Se caracterizaron sus propiedades en bulto y se determinaron sus reconstrucciones de superficie más estables. Se proponen los primeros modelos en existencia de las complejas superficies del α-Mn y el comportamiento de los momentos magnéticos de la superficie más estable es discutido. Se compararon imágenes de STM experimentales y teóricas de las reconstrucciones de filas y cuadros y se encontró que están en excelente acuerdo. También se examinó el papel que juega la difusión de C en el incremento magnético de las superficies de D0_{22}-Mn_3Ga. Se discute esto en términos del efecto de superficie, el efecto magnetoelástico, la interacción de superintercambio y la Densidad de Estados de cada átomo. Finalmente, se estudiaron dos reconstrucciones de superficie del L1_0-MnGa con periodicidades 1×2 terminadas en Ga. Se discuten sus propiedades magnéticas en términos del efecto de superficie, la Densidad de Estados de cada átomo y la densidad de magnetización. Se determinó que la reconstrucción terminada en Cu podría fungir como un catalizador de Aleación de un Sólo Átomo magnético.

Palabras clave: Teoría del Funcional de la Densidad, reconstrucciones de superficie, estructura electrónica, anisotropía magnetica

Dedication

A mi mamá, por formarme.

A mi papá, por siempre apoyarme.

A mis hermanos, por estar siempre.

A mi prometida, Patsy, por hacerme un mejor hombre.

Te amo.

Acknowledgements

To the Center for Scientific Research and Higher Education at Ensenada for helping me obtain all the resources to prepare myself professionally and be able to carry out this project.

To the National Council of Science and Technology (CONACyT, by its acronym in Spanish) for providing me with the economic support to carry out my master's studies (Scholarship No.: 20274657, CVU: 1039137), as well as to carry out the research with the A1-S-9070 scholarship.

To the National Autonomous University of Mexico for providing me with education at the undergraduate level, as well as providing financial support to carry out the research through the DGAPA-PAPIIT IN105722, IA100822, IN110820, and IG200320 grants; as well as LANCAD-UNAM-DGTIC-051, LANCAD-UNAM-DGTIC-368, and LANCAD-UNAM-DGTIC-150.

To all the centers and institutes that lent their computing resources to carry out the calculations: the National Supercomputing Laboratory of Southeast Mexico (LNS, by its acronym in Spanish) and the THUBAT KAAL National Supercomputing Center of the Potosino Institute of Scientific and Technological Research (IPICYT, by its acronym in Spanish).

To all the individuals who provided technical assistance and helpful discussions: Eduardo Murillo Bracamontes, Aldo Rodríguez Guerrero, Marina Mendoza Núñez, Luis Gerardo Reyes Sánchez, and especially to Dr. Perry Corbett for his experimental contribution to the study of α-Mn surfaces.

Finally, to all the members of the Virtual Laboratory of Materials Modeling (LVMM, by its acronym in Spanish), in particular to Dr. Noé Fernández, Dr. Rodrigo Ponce, Dr. Noboru Takeuchi, and my thesis advisor and friend Dr. Jonathan Guerrero, for their willingness to share their knowledge with me, answer questions, and allow me to be part of the research group. Without your support this project would not have been possible.

From the research carried out in this thesis, there are two manuscripts and one published article (https://doi.org/10.1016/j.apsusc.2022.153514). The results have been presented at the following conferences: Fall Meeting 2021 of the Materials Research Society and the APS March Meeting 2022.

Table of contents

Table of contents (continuation)

List of figures

Figure Page

List of figures (continuation)

Figure Page

List of figures (continuation)

List of tables

Chapter 1. Introduction

The study of the properties of the elements that make up the universe is one of the main objectives of the physical-chemistry. One of the most outstanding achievements of this branch of science was done by Dimitri Mendeleev during the second half of the XIX century, when he presented his table to organize the elements periodically according to their properties (Hargittai and Hargittai, 2019). This table allows us to predict properties of interest of the elements, such as the metallic character, electronic configuration, magnetic behavior, or even the crystal structure.

From a structural point of view, manganese (Mn) is possibly the most complicated element in existence. It is located in the d-block and VII-group of Mendeleev's periodic table, and due to this, we could be tempted to think that it has either an HCP, FCC, or BCC crystal structure, like any of its neighbor elements (Preuss et al., 1974, pp. 29—45). However, all of these assumptions are entirely wrong. In fact, Mn has a unique and complex crystal structure that is illustrated in **Figure 1** and will be explained later in this thesis.

Mn is the twelfth most abundant element in Earth's crust (Emsley, 2011, pp. 249–253) and it is mainly mined in South Africa, Australia, China, Brazil, and India (Elliott et al., 2018). It finds its main application in the metallurgic industry, where approximately 85 % of the world's Mn is used for the fabrication of steels (Zhang and Cheng, 2007). Two prime examples of this are Mushet's and Hadfield's steels, which were named after their discoverers. They are types of alloy steels with small amounts of Mn that are more malleable and much more tolerant to strains in comparison to other steels, respectively (H. W. H., 1927). Manganese's second most popular application is also found in the metallurgic industry for aluminum alloys. Aluminum with a Mn-percentage between 0.8 and 1.5 % presents greater corrosion resistance and is used to fabricate cans for beverages. It is estimated that by the year 2000, around 16,000 tons of Mn had been used for this purpose (Kaufman, 2000, pp. 93–94).

There are several other applications for Mn in different compounds. For example, manganese oxide (IV) is used as a catalyst, as an additive in rubber and fertilizers, and as a reagent in textile printing (Encyclopedia Britannica, 2010; Wirth, 2013). Manganese sulfate is added to soils to promote plant growth, especially in citrus crops. It is an excellent reducing agent, particularly useful in the manufacture of paint and varnish dryers (Royal Society of Chemistry, 2021). Etc.

However, let us shift our focus back to the metallurgic applications of Mn, specifically towards the manganese-gallium (Mn-Ga) alloys. By combining these two elements, we obtain materials with prop-

erties suitable for applications in spintronic devices. Spintronic devices — which distinguish between spin-up and spin-down carriers — are very much like electronic devices, only that they have an added degree of freedom, which, until now, has barely been technologically exploited to our advantage. For instance, Mn-Ga alloys can be used to create Magnetic Tunnel Junctions (MJTs). These are typical spintronic devices that consist of a non-magnetic (NM) insulating barrier separating two ferromagnetic (FM) or ferrimagnetic (fM) metal electrodes that exhibit a large resistance change depending on magnetization states of the electrodes (Ma et al., 2014). Mn-Ga alloys are typically FM and exhibit properties that make them appealing to be the metal electrodes on MJTs. There are several other important technologies based on MJTs — such as Hard Disk Drives (HDD) and Magnetoresistive Random-Access Memories (MRAM) — which have existed for a while, but are still being researched because they are proposed to surpass competing technologies and become a universal memory (Åkerman, 2005). Even so, the implementation of Spin-Transfer Torque (STT)-MRAM technology in the main and low-level memories of computers is predicted to allow the creation of revolutionary instant-on and normally-off computers (Ando et al., 2014).

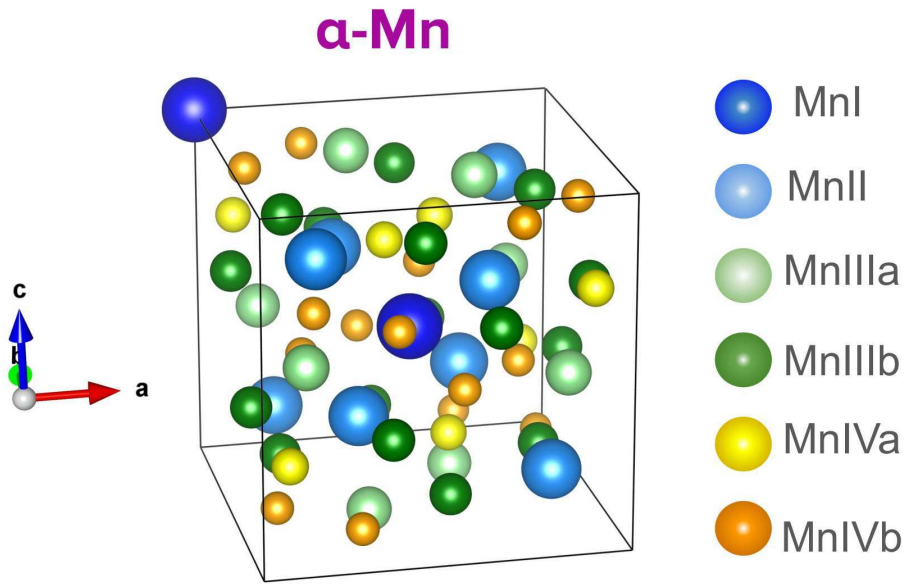

Figure 1. Magneto-crystalline structure of α-Mn. The atoms in non-equivalent sites are represented with different colors: MnI (dark blue), MnII (clear blue), MnIIIa (turquoise), MnIIIb (green), MnIVa (yellow) and MnIVb (orange). Image based on the article by Hobbs et al. (2003).

Seeking different materials which will fit these applications is not only for the sake of curiosity. It was speculated by Lewis and Jiménez-Villacorta (2013) that governments will likely exercise tighter restrictions on rare earth exports (the most commonly used elements for MRAM applications) in an attempt to clean up existing environmental issues and attend to their domestic economic priorities.

Mn-Ga alloys find another application in the creation of semiconductor-magnetic hybrid devices. Inside these devices, the magnetic field affects the electrons in the semiconductor by either shifting the energy of electronic levels or acting directly on the carriers. This effect could be harnessed for the creation of magneto-electronic devices, such as notch filters or spin injection devices (Prinz, 1990); or the creation of magneto-optical devices such as spin light-emitting diodes (Wang et al., 2009; Grunebohm et al., 2009).

In this sense, Heusler-like D0$_{22}$-Mn$_3$Ga and L1$_0$-MnGa alloys are very attractive due to their versatile magnetic properties. They are alloys with approximately 25 and 50 % Ga concentration in the Mn-Ga phase diagram (see **Figure 2(a)**), respectively. At the left extreme of **Figure 2(a)** is located the α-Mn phase, with 0 % Ga content. Both D0$_{22}$-Mn$_3$Ga and L1$_0$-MnGa alloys possess a high Curie temperature, spin polarization, coercivity, and Perpendicular Magnetic Anisotropy (PMA) (Ma et al., 2013, 2014), which make them excellent candidates for fabricating rare-earth-free magnets and spintronic devices (Katine and Fullerton, 2008; Yuasa et al., 2013).

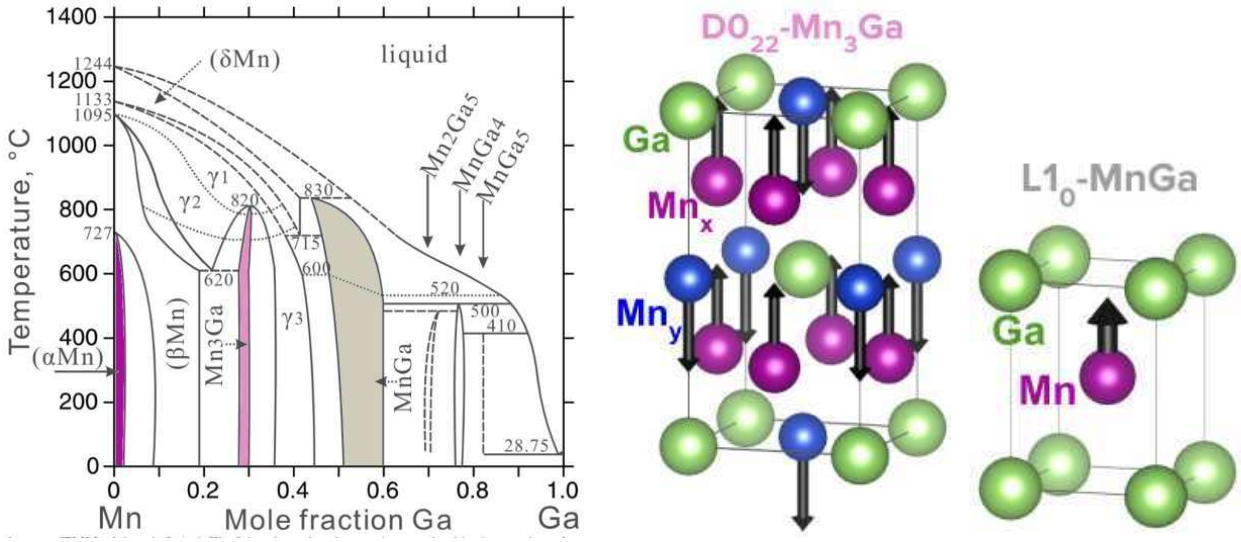

(a) (b) (c)

Figure 2. Representation of various Mn-Ga alloys: (a) Mn-Ga phase diagram and magneto-crystalline structures of (b) D0$_{22}$-Mn$_3$Ga and (c) L1$_0$-MnGa. The atoms are represented with different colors in the different models: Ga (turquoise), Mn$_x$ (purple), and Mn$_y$ (dark blue) for the D0$_{22}$-Mn$_3$Ga; and Ga (turquoise) and Mn (purple) for L1$_0$-MnGa; respectively. The phase diagram was adapted from the article by Hao and Xiong (2020).

In the present thesis, first-principles computational simulations were performed to study the structural, electronic, and magnetic properties of the three aforementioned Mn-Ga alloys — α-Mn, D0$_{22}$-Mn$_3$Ga, and L1$_0$-MnGa — under different conditions using Density Functional Theory (DFT).

1.1 Background

One of the most important characteristics of Mn is its electronic configuration since all of the electrons in its 3d orbitals are unpaired. This allows Mn (in principle) to have a larger magnetic moment than any other element and is one of the key factors in explaining its crystal structure (Hobbs et al., 2003). In fact, once the crystal structure of α-Mn was discovered, several researchers took upon the task of completing the description of this crystal by studying its magnetic behavior. Bradley and Thewlis (1927) discovered that elemental Mn has three crystal structures, which they baptized as α, β and γ — being α-Mn the most stable one. It belongs to the $I\bar{4}3m$ space group and has a unit cell with 58 atoms placed in 6 nonequivalent magnetic sites (see **Figure 1**). Later on, three articles were published reporting neutron diffraction measurements at different temperatures and synthesis conditions (Shull and Wilkinson, 1953; Kasper and Roberts, 1956; Oberteuffer et al., 1968), in which the magnetic moments of the Mn atoms were estimated erroneously assuming a collinear antiferromagnetic model (CL-AFM) with only 4 types of atoms in the α-Mn cell (see **Figure 3(a)**).

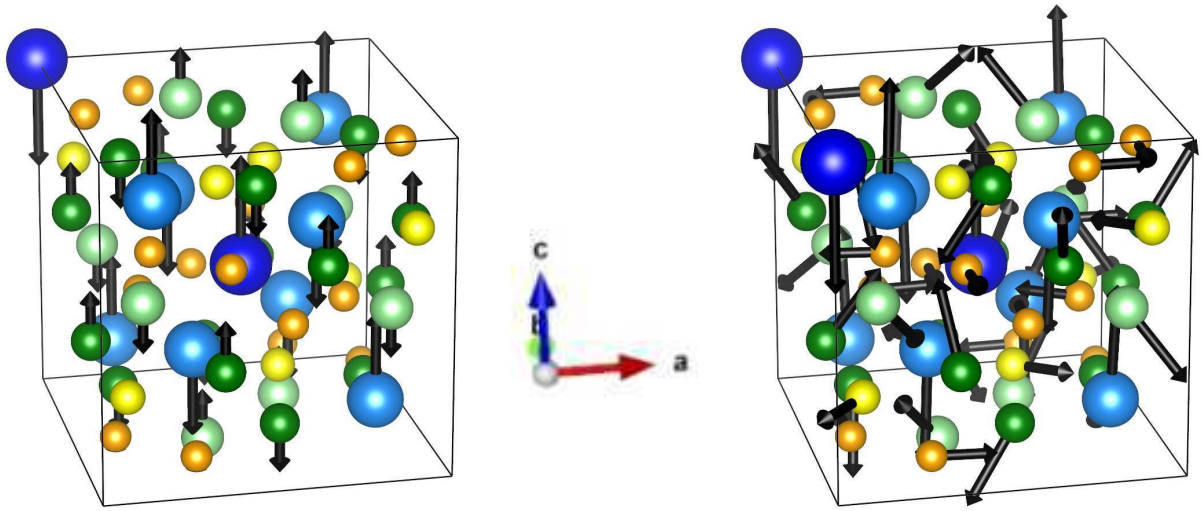

(a) (b)

Figure 3. Different magnetic orders for the α-Mn structure: (a) CL-AFM and (b) NCL-AFM. The atoms placed in nonequivalent sites are represented with the same colors as in **Figure 1**. The values of the magnetic moments in (a) were taken from (Oberteuffer et al., 1968) and in (b) from (Lawson et al., 1994), respectively.

A couple of years later, the first systematic investigation of the Mn-Ga phase diagram over the whole composition range was performed by Meissner et al. (1965). They reported 10 intermetallic compounds — among them the α-Mn, Mn_3Ga, and MnGa — and determined that the strukturbericht designation of MnGa is $L1_0$. In the same year, Wachtel and Nier (1965) also determined the Mn–Ga phase diagram but

determined the limits of the phases based on the measurement of the magnetic susceptibility. Further studies were performed on the Mn-Ga phase diagram giving consistent results for the three structures mentioned above (Masumoto et al., 1978; Lu et al., 1980; Minakuchi et al., 2012; Tillard and Belin, 2012).

Then, in the quest for characterizing the magnetic moments of the α-Mn structure with the highest possible precision, Kunitomi et al. (1969); Yamada et al. (1970) published a couple of reports where they synthesized α-Mn mono-crystals and took neutron diffraction measurements of them. They compared their results with the theoretical values of intensities based on the collinear model for the magnetic moments and found that this model did not correctly explain the experimental measurements. So they proposed a model with 6 magneto-crystallographically distinct atoms (see **Figure 3(b)**) and a noncollinear antiferromagnetic (NCL-AFM) behavior of the magnetic moments. The validity of this model was confirmed by Yamagata and Asayama (1972), where they used nuclear magnetic resonance to study the α-Mn structure. In addition, Lawson et al. (1994) performed time-of-flight neutron-diffraction measurements (a method derived from regular neutron diffraction) and arrived at the same conclusion.

With the evolution of computational technology and the development of methods based on first-principles, more tools became available to study these types of systems. To mention some examples, Sliwko et al. (1994) reported the electronic properties of α-Mn by applying DFT, and Hobbs et al. (2003) also used DFT to study, among other things, the relationship between the magnetic moment of the atoms with other properties of α-Mn. There is a cornucopia of theoretical and experimental articles researching both the crystallographic and magnetic properties of the $D0_{22}$-Mn_3Ga and $L1_0$-MnGa alloys. To mention some, $D0_{22}$-Mn_3Ga belongs to the $I4/mmm$ space group (Krén and Kádár, 1970), is fM (see **Figure 2(b)**), has a Courie temperature above $730\ K$ (Balke et al., 2007), and its coercivity can be as large as $18.2\ kOe$ (Wei et al., 2014). $L1_0$-MnGa belongs to the $P4/mmm$ space group (Mix et al., 2015), is FM (see **Figure 2(c)**), and its PMA constant can reach values as high as $22 - 27\ Merg/cm^3$ (Al-Aqtash and Sabirianov, 2015), which are also tunable by an appropriate choice of substrate and growth conditions (Zha et al., 2011; Zhu et al., 2012, 2013).

As attractive as the magnetic properties of $D0_{22}$-Mn_3Ga and $L1_0$-MnGa are, they are not good enough by themselves to successfully be applied to new devices. Several strategies have been attempted to "improve" their magnetic properties for this end. Brown et al. (2016a) applied a magnetic field during the heat treatment process of $D0_{22}$-Mn_3Ga and found that this process increased the remanence up to 50 % over the non-magnetic field annealed system and increased the coercivities up to 19.4 kOe (the highest coercivity reported in bulk Mn-Ga samples). Brown et al. (2016b) tested the effect of doping the

structure with Bi, Al, Fe and B atoms, finding high coercivities up to 16.6 kOe and remanence increased by 115 % over the binary system. Thin films of $L1_0$-MnGa have also been thoroughly studied. Ma et al. (2013) characterized the structural and magnetic properties of the MnGa-based MTJs and discussed the dependence of composition and interlayer thickness on the magnetoresistance ratio with different core structures. Also, the effect of inserting a Mn layer with a MgO barrier on the magnetoresistance ratio of MnGa MTJs was evaluated (Suzuki et al., 2018). Mao et al. (2017) reported that the addition of Co_2MnSi interlayers fully perpendicularize the MnGa/MgO MTJs by solving the lattice mismatch and surface energy restrictions. These are just different approaches to the same problem: make these alloys more applicable.

1.2 Justification

The previously mentioned studies have contributed to the scientific heritage of Mn-Ga alloys, but there is still much room for research in this area. There are virtually no articles that focus on the surface properties of the α-Mn structure. Wulfhekel and Gao (2010) published a review article in which they discuss the differences between the Scanning Tunneling Microscopy (STM) methods for FM, CL-AFM, and NCL-AFM materials. Although the STM images and the behavior of the magnetic moments on the (001) surface of α-Mn are analyzed in this article, nothing is said there nor in the rest of the literature about the possible surface reconstructions nor the rest of their properties.

In addition, it is worth mentioning that there also exist several databases obtained from DFT calculations that contain many properties of the α-Mn structure. The most prominent example of this is the Materials Project (Jain et al., 2013; Materials Project, 2013a) website, which includes properties such as the Surface Formation Energy (SFE) and the Wulff shape of this material (Tran et al., 2016). However, no database shows a comprehensive analysis of the properties of element surfaces. The motivation for this part of the project is that (thanks to a collaboration) our research group possesses experimental STM images of α-Mn surfaces. Because of this, we performed the computational part of a theoretical-experimental study that characterizes them for the first time.

On the other hand, there are some recent studies on $D0_{22}$-Mn_3Ga and $L1_0$-MnGa of particular interest for the present thesis. Gutiérrez-Pérez et al. (2017); Holguín-Momaca et al. (2019) performed two theoretical-experimental studies evaluating the effect of interstitial carbon (C) atoms in the electronic and magnetic properties of $D0_{22}$-Mn_3Ga bulks. The present thesis presents a theoretical study on the effect of C in this structure, but this time taking into consideration the different (001) surface recon-

structions. Regarding $L1_0$-MnGa, Corbett et al. (2017) studied its surface reconstructions and described a 1×2 Ga-terminated surface with a Mn-by-Ga substitution, driving to a row structure orthogonal to the $[001]$ axis. This thesis proposes a Cu-induced surface reconstruction of that structure that potentially adds yet another item to the list of applications to Mn-Ga alloys: heterogeneous catalysis. The main goal of studying these two materials is to provide more information regarding their properties and get closer to innovating the previously-mentioned technologies with the application of these materials.

1.3 Hypothesis

"The surface reconstructions of Mn-Ga alloys exhibit different electronic and magnetic properties than the bulk."

1.4 Objectives

1.4.1 General objectives

Perform first-principles calculations to characterize the structural, electronic, and magnetic properties of the most stable surface reconstructions of the α-Mn, $D0_{22}$-Mn_3Ga, and $L1_0$-MnGa.

1.4.2 Specific objectives

- Perform a structural optimization of the bulks in different magnetic orders of the three Mn-Ga alloys.
- Propose different surface reconstructions in the (001) surface of the three Mn-Ga alloys.
- Determine the most stable reconstructions of the three Mn-Ga alloys by comparing their surface formation energies.
- Obtain theoretical STM images of the most stable surface reconstructions of the α-Mn and $L1_0$-MnGa.
- Calculate the electronic density of states of the most stable reconstructions of the $D0_{22}$-Mn_3Ga and $L1_0$-MnGa.

- Analyze the behavior of the magnetic moments of the most stable reconstructions of the three Mn-Ga alloys.
- Compare results with existing literature.

Chapter 2. Theoretical framework

Nowadays, DFT is the standard quantum mechanical tool to perform computational simulations of materials. It provides a method to describe the electron interactions in any material and predict its properties based solely on first principles. This compelling theory is based on several pillars of quantum mechanics, which shall be reviewed:

2.1 The Schrödinger equation

The Schrödinger equation is one of the pillars of quantum mechanics. It allows its user to find the energies (E) and wave functions (Ψ) of any quantum system, which are defined as orthonormal for simplicity. Considering a system with M nuclei and N electrons, this equation can be expressed as:

$$\widehat{H}\Psi\left(\boldsymbol{r_1}, s_1, \cdots, \boldsymbol{r_N}, s_N, \boldsymbol{R_1}, \cdots, \boldsymbol{R_M}\right) = E\Psi\left(\boldsymbol{r_1}, s_1, \cdots, \boldsymbol{r_N}, s_N, \boldsymbol{R_1}, \cdots, \boldsymbol{R_M}\right) \tag{1}$$

where $\widehat{H}$ is the Hamiltonian operator, $\boldsymbol{r_k}$ (and s_k) represent the spatial (and spin) coordinates of the kth electron, respectively (bold symbols represent a vector entity), and $\boldsymbol{R_k}$ represents the spatial coordinates of the kth nucleus (Koch and Holthausen, 2001, p. 1). $\widehat{H}$ can be expressed (in atomic units) in terms of different energy contributions as follows:

$$\widehat{H} = -\frac{1}{2}\sum_{i=1}^{N}\boldsymbol{\nabla_i}^2 - \frac{1}{2}\sum_{A=1}^{M}\frac{\boldsymbol{\nabla_A}^2}{M_A} - \sum_{i=1}^{N}\sum_{A=1}^{M}\frac{Z_A}{|\boldsymbol{r_i} - \boldsymbol{R_A}|} + \sum_{i=1}^{N}\sum_{j>i}^{N}\frac{1}{|\boldsymbol{r_i} - \boldsymbol{r_j}|} + \sum_{A=1}^{M}\sum_{B>A}^{M}\frac{Z_A Z_B}{|\boldsymbol{R_A} - \boldsymbol{R_B}|} \tag{2}$$

where the different terms (in order of appearance) describe the kinetic energies of the electrons ($\widehat{T}_e$) and the nuclei ($\widehat{T}_n$), the electrostatic energy due to electron-nucleus attraction ($\widehat{V}_{ne}$), due to electron-electron repulsion ($\widehat{V}_{ee}$), and due to nucleus-nucleus repulsion ($\widehat{V}_{nn}$). $\boldsymbol{\nabla}^2$ represents the Laplacian operator and A, B count through the nuclei while i, j do it through the electrons in the system.

Equation (1) can only be solved analytically for a minimal number of cases (Hodgson, 2021; Scott and Zhang, 2015; Sever et al., 2008; Busch et al., 1998; Ishkhanyan, 2015; Sinitsyn and Chernyak, 2017). For most physical and chemical systems, the Schrödinger equation becomes impossible to solve. However, this has not halted researchers from solving more complex quantum systems. The general approach is to perform some mathematical approximation to the Schrödinger equation that will result in a satisfactory degree of accuracy.

2.2 Variational principle

Before going over approximations that lead to the current state of DFT, let us talk about the variational principle. It is a tool borrowed from the calculus of variations, which involves finding functions that optimize the values of quantities that depend on those functions. Particularly in quantum mechanics, what we mean by "solving" the Schrödinger equation is to find its eigenvalues and eigenfunctions at the ground state (E_0, Ψ_0). However, one must remember that equation 1 holds for any orthonormal wave function, not just the ground state. All the other wave functions (Ψ) are considered excited states of the system, and their energies (E) are upper bounds to the ground-state energy (Griffiths, 1995, pp. 256, 261). This is, in essence, the variational principle; and can be mathematically stated as follows:

$$\left\langle \Psi \middle| \widehat{H} \middle| \Psi \right\rangle = E > E_0 = \left\langle \Psi_0 \middle| \widehat{H} \middle| \Psi_0 \right\rangle \tag{3}$$

With the help of the variational principle, the Schrödinger equation can be solved iteratively until reaching a satisfactorily close solution. Even if Ψ has no relation to the actual wave function, one often gets miraculously accurate values for E (Griffiths, 1995, p. 261). But of course, if you have some way of guessing a realistic wave function (which we shall see in this chapter), the better.

2.3 Born-Oppenheimer approximation

This is the first and most simple approximation for solving the Schrödinger equation. It is also known as the "clamped-nuclei approximation" and stems from two facts:

- The charges of the electrons and protons have the same magnitude; therefore the electrostatic forces experienced by nuclei and electrons must have the same magnitude.
- The mass of the electron is much smaller than that of the nucleus — 1836 times for the H atom and more for the other atoms.

By taking together the previous statements, it follows that the speed of the nuclei must be much smaller than that of the electrons. The Born-Oppenheimer approximation consists in actually neglecting the speed of the nuclei and considering them fixed in space (Koch and Holthausen, 2001, pp. 4–5). That means that the kinetic energy term of the nuclei becomes zero $(\widehat{T}_n \to 0)$ and the repulsive

potential among the nuclei becomes a constant ($\widehat{V}_{nn} \rightarrow V_{nn}$). Furthermore, it is grouped with $\widehat{V}_{ne}$ and any external electromagnetic fields in the so-called external potential ($\widehat{V}_{ext}$). This approximation also eliminates the nuclei dependence of the wave function: $\Psi\left(\boldsymbol{r_1}, s_1, \cdots, \boldsymbol{r_N}, s_N, \boldsymbol{R_1}, \cdots, \boldsymbol{R_M}\right) \rightarrow \Psi\left(\boldsymbol{r_1}, s_1, \cdots, \boldsymbol{r_N}, s_N\right)$. Considering all of this, equation (1) can be expressed as:

$$\widehat{H}\left|\Psi\right\rangle = \left(\widehat{T}_e + \widehat{V}_{ee} + \widehat{V}_{ext}\right)\left|\Psi\right\rangle = E\left|\Psi\right\rangle \tag{4}$$

This approximation, although very simple, enables solving the Schrödinger equation for more complex systems, but other approximations are further required to reach the current state of the art.

2.4 Hartree and Hartree-Fock approximations

The Hartree approximation assumes beforehand that the wave function of the system is a product (also known as Hartree product) of N one-electron wave functions ($\psi_1, \psi_2, ..., \psi_N$), as follows:

$$\Psi\left(\boldsymbol{r_1}, s_1, \cdots, \boldsymbol{r_N}, s_N\right) = \psi_1\left(\boldsymbol{r_1}, s_1\right)\psi_2\left(\boldsymbol{r_2}, s_2\right)\cdots\psi_N\left(\boldsymbol{r_N}, s_N\right) \tag{5}$$

By substituting equation (5) in (1) one can implement the separation-of-variables method to derive a set of N coupled differential equations. The solution of these equations yields the Hartree wave function and energy of the system. However, there is one fundamental flaw with Hartree's model: it does not consider Pauli's exclusion principle. This principle says that particles of half-integer spin must have antisymmetric wave functions so that they vanish if two particles occupy the same state (Nave, 2000). This consideration was implemented in the Hartree-Fock approximation. Instead of the Hartree product, the wave function has the shape of a Slater determinant:

$$\Psi\left(\boldsymbol{r_1}, s_1, \cdots, \boldsymbol{r_N}, s_N\right) = \frac{1}{\sqrt{N}}\begin{vmatrix} \psi_1\left(\boldsymbol{r_1}, s_1\right) & \psi_2\left(\boldsymbol{r_1}, s_1\right) & \cdots & \psi_N\left(\boldsymbol{r_1}, s_1\right) \\ \psi_1\left(\boldsymbol{r_2}, s_2\right) & \psi_2\left(\boldsymbol{r_2}, s_2\right) & \cdots & \psi_N\left(\boldsymbol{r_2}, s_2\right) \\ \vdots & \vdots & \ddots & \vdots \\ \psi_1\left(\boldsymbol{r_N}, s_N\right) & \psi_2\left(\boldsymbol{r_N}, s_N\right) & \cdots & \psi_N\left(\boldsymbol{r_N}, s_N\right) \end{vmatrix} \tag{6}$$

The proposed wave function complies with the principle of antisymmetry because it is a property of the determinants that exchanging rows or columns changes the sign of a determinant (Schay, 2012, pp. 223–224).

2.5 Electron density

So far, we have a Schrödinger-like equation stating the wave function explicitly. This function is a close approximation and can now be solved. However, this is easier said than done. Even a one-electron wave function is a function of the electron's three spatial coordinates and three spin coordinates. If we add a couple of tens or hundreds of electrons (something very reasonable if you want to model anything larger than an atom), then this function becomes unbearably complex and its solution, although is technically possible, becomes computationally impossible. Just to put things in perspective, if we wanted to write the wave function of an aluminum atom, in real space, on a computer file, considering only the electronic degrees of freedom and a coarse real space grid of only 100 points in each dimension, a hard disk the size of the milky way would not be big enough (Sottile and Reining, 2021b).

The electron density provides us with a miraculous solution to this problem since it only depends on the three spatial coordinates of the system (Koch and Holthausen, 2001, pp. 29–31). It is related to the wave function as follows:

$$\rho\left(\boldsymbol{r}\right)=\rho\left(\boldsymbol{r_1}\right)=N\int\cdots\int\left|\Psi\left(\boldsymbol{r_1},s_1,\cdots,\boldsymbol{r_N},s_N\right)\right|^2ds_1d\boldsymbol{r_2}ds_2\cdots d\boldsymbol{r_N}ds_N \tag{7}$$

where $\rho\left(\boldsymbol{r}\right)$ gives us the probability of finding an electron in the volume element $d\boldsymbol{r_1}$ with an arbitrary spin. Strictly speaking, $\rho\left(\boldsymbol{r}\right)$ is a probability density, but it is commonly called an electron density.

Also, it is worth noting that the electron density can provide us with all the information needed to fully describe the Hamiltonian of any system. This is because we can obtain the number of electrons and the atomic number from $\rho\left(\boldsymbol{r}\right)$ by performing an inner product in equation (7) — and remembering that the wave functions are orthonormal — and thanks to Kato's cusp condition (Kato, 1957; March, 1986), respectively. These go as follows:

$$\int\rho\left(\boldsymbol{r}\right)d\boldsymbol{r_1}=\int\rho\left(\boldsymbol{r_1}\right)d\boldsymbol{r_1}=N\int\cdots\int\left|\Psi\left(\boldsymbol{r_1},s_1,\cdots,\boldsymbol{r_N},s_N\right)\right|^2d\boldsymbol{r_1}ds_1\cdots d\boldsymbol{r_N}ds_N=N \tag{8}$$

$$\left.\frac{\partial\rho\left(\boldsymbol{r}\right)}{\partial r}\right|_{\boldsymbol{r}\to\boldsymbol{R}}=-2Z\rho\left(\boldsymbol{R}\right) \tag{9}$$

2.6 Hohenberg–Kohn theorems

Hohenberg-Kohn's (HK) theorems laid the foundation for creating DFT. The first theorem of Hohenberg and Kohn (1964) formally describes the total energy as a unique functional of the electron density. This is extremely important since it means that the wave function and all its observables can also be expressed in terms of electron density, rendering the solution of the Schrödinger equation computationally solvable. The first HK theorem is mathematically expressed as follows:

$$\widehat{H}\left[\rho\left(\boldsymbol{r}\right)\right] = \int \rho\left(\boldsymbol{r}\right) V_{ext}\left(\boldsymbol{r}\right) d\boldsymbol{r} + \widehat{T}_e\left[\rho\left(\boldsymbol{r}\right)\right] + \widehat{V}_{ee}\left[\rho\left(\boldsymbol{r}\right)\right] \tag{10}$$

where the external potential operator ($\widehat{V}_{ext}$) is expressed explicitly in terms of the electron density. Notice how the Hamiltonian is a function of the electron density, which is a function of the position. This function of a function is mathematically called a functional (Weisstein, Eric W., 2022). Being all of the observables functionals of the electronic density, this is where the name of the theory comes from: Density Functional Theory.

The second HK theorem demonstrates that the variational principle holds with the density functional as the primary variable. In equation form, this theorem can be written as:

$$E\left[\rho\left(\boldsymbol{r}\right)\right] > E\left[n_0\left(\boldsymbol{r}\right)\right] \tag{11}$$

Basically, equation (11) states that the electron density that minimizes the energy of the global functional is the exact ground-state electron density, corresponding to the complete solutions of the Schrödinger equation (Frijns et al., 2021). HK's theorems establish the base for what DFT is, but they are not enough because they are still not analytically solvable. The expressions for the second and third terms in equation (10) are still not known to date, rendering the analytical solution still impossible.

2.7 Kohn-Sham formulation

Thanks to the Kohn-Sham (KS) formulation, solving the Schrödinger equation for complex systems finally became possible (Sottile and Reining, 2021a). In it, Kohn and Sham (1965) introduced a fictitious supporting system of non-interacting electrons that has the same electron density as the interacting system. Their article demonstrated that this statement indeed makes sense and provided the expressions to find the electron density. KS introduced an expression for the Hamiltonian in equation 10 that

separates the known interactions from the unknown contributions of an interacting system of electrons. It defines the Hamiltonian of the system as follows:

$$\widehat{H}\left[\rho\left(\boldsymbol{r}\right)\right]=\int\rho\left(\boldsymbol{r}\right)V_{ext}\left[\rho\left(\boldsymbol{r}\right)\right]d\boldsymbol{r}+\frac{1}{2}\int\int\frac{\rho\left(\boldsymbol{r}\right)\rho\left(\boldsymbol{r'}\right)}{\left|\boldsymbol{r}-\boldsymbol{r'}\right|}d\boldsymbol{r}d\boldsymbol{r'}+\widehat{T}_s\left[\rho\left(\boldsymbol{r}\right)\right]+\widehat{E}_{XC}\left[\rho\left(\boldsymbol{r}\right)\right] \tag{12}$$

where the first term is the external potential ($\widehat{V}_{ext}$), the second term is the classical electrostatic Hartree energy of the non-interacting electrons ($\widehat{V}_H$), $\widehat{T}_s$ is the kinetic energy of a system of non-interacting electrons, and $\widehat{E}_{XC}$ is the exchange and correlation energy of an interacting system — which accounts for the contribution of all the complex interactions among electrons. Its expression in terms of the energy contributions established in equation 10 is:

$$\widehat{E}_{XC}\left[\rho\left(\boldsymbol{r}\right)\right]=\widehat{T}_e\left[\rho\left(\boldsymbol{r}\right)\right]-\widehat{T}_s\left[\rho\left(\boldsymbol{r}\right)\right]+\widehat{V}_{ee}\left[\rho\left(\boldsymbol{r}\right)\right]-\widehat{V}_H\left[\rho\left(\boldsymbol{r}\right)\right] \tag{13}$$

No analytical expression for the exchange-correlation energy exists. Some of the existing approximations and their applications will be covered in the next section. Finally, after performing a variational optimization via Lagrange multipliers in equation (12), we can obtain the famous KS equations. These are a set of N Schrõdinger-like equations for non-interacting electrons that together give the exact electron density of the interacting system. The KS equation for the ith electron is:

$$\left(-\frac{1}{2}\boldsymbol{\nabla}^2+V_{ext}\left(\boldsymbol{r}\right)+\int\frac{\rho\left(\boldsymbol{r'}\right)}{\left|\boldsymbol{r}-\boldsymbol{r'}\right|}d\boldsymbol{r'}+\frac{\partial\widehat{E}_{XC}\left[\rho\left(\boldsymbol{r}\right)\right]}{\partial\rho\left(\boldsymbol{r}\right)}\right)\psi_i\left(\boldsymbol{r},s_i\right)=\epsilon_i\psi_i\left(\boldsymbol{r},s_i\right) \tag{14}$$

where the last three terms inside the parenthesis are often called the effective or KS potential ($\widehat{V}_{KS}$). This equation yields the exact same electron density as the real interacting system, which can be expressed as:

$$\rho\left(\boldsymbol{r}\right)=\sum_i^N f_i\left\langle\psi_i\left(\boldsymbol{r},s_i\right)\left|\psi_i\left(\boldsymbol{r},s_i\right)\right.\right\rangle \tag{15}$$

where f_i is the occupation of the ith orbital (Capelle, 2006).

Now, in equation (14) we can see that $\widehat{V}_{KS}$ depends on ρ, which we know thanks to equation (15) that depends on ψ_i. But wait a minute, finding the expressions for ψ_i is the same as solving equation (14), for which we must know the expression for $\widehat{V}_{KS}$. We have come back to the beginning. This means that solving the KS equations is a cyclical problem. The usual way of solving it is called the "self-consistency cycle." It consists of making an initial guess for $\rho\left(\boldsymbol{r}\right)$ (usually using a Slater determinant), calculating the corresponding $\widehat{V}_{KS}\left[\rho\left(\boldsymbol{r}\right)\right]$, and then solving equation (14) for the ψ_i. From these, we calculate a new electron density using equation (15), and start again, repeating the process until reaching convergence.

By "reaching convergence" we mean that, thanks to the variational principle, the results can be as precise as your computer systems allow you to, but they will never reach the exact ground state. Therefore a convergence threshold is established. Once the energy varies no more than $10^{-4}\ eV$ and the forces no more than $10^{-3}\ eV/$Å between each step of the calculation is one of the standards (Kresse and Furthmüller, 2022a,b). However, one can choose among many different criteria (Nemec and Hofmann, 2014): final energy, electron density, force, sum of eigenvalues, etc. With a correct selection of parameters, the calculations rarely require more than a couple of dozen iterations to achieve convergence (Capelle, 2006).

2.8 Exchange-correlation approximations

Several approximations have been developed for the exchange-correlation term of the KS potential, namely, the Local Density Approximation (LDA), Generalized Gradient Approximation (GGA), extensions of it (meta-GGA and hyper-GGA), and hybrid functionals (Harun et al., 2020). Each of these approximations has a different approach to the exchange-correlation term and is thus suitable for a specific type of material. Generally speaking, LDA and GGA are the most widely used types of approximations for DFT. Roughly speaking, they are similar to a Taylor series of a function. They seek to approximate the exchange-correlation term using differential operators of different orders at a certain point. The LDA functionals depend only on the electron density, while the GGA ones depend on both the density and its first-order differential operator (Capelle, 2006). There are dozens of variations of those two expressions, but they can be expressed in general as:

$$\widehat{E}_{XC}^{LDA}\left[\rho\left(\boldsymbol{r}\right)\right] = \int \rho\left(\boldsymbol{r}\right)\epsilon_{XC}^{LDA}\left[\rho\left(\boldsymbol{r}\right)\right]d\boldsymbol{r} \tag{16}$$

$$\widehat{E}_{XC}^{GGA}\left[\rho\left(\boldsymbol{r}\right)\right] = \int \rho\left(\boldsymbol{r}\right)\epsilon_{XC}^{GGA}\left[\rho\left(\boldsymbol{r}\right),\boldsymbol{\nabla}\rho\left(\boldsymbol{r}\right)\right]d\boldsymbol{r} \tag{17}$$

where ϵ_{XC}^{LDA} and ϵ_{XC}^{GGA} are the exchange-correlation energies per particle of a homogeneous electron gas.

Hybrid functionals are a linear combination of the exact exchange energy from Hartree-Fock theory with the rest of the exchange-correlation energy coming from other sources. Different proportions of different functionals mean a different behavior. Not surprisingly, calculations with these functionals are computationally more expensive, hence why they are only used when absolutely necessary, such as in semiconductor systems (Flores et al., 2018) or to study the organic thermochemistry and reactivity (Lu et al., 2013). Particularly for magnetic metals, the Perdew–Burke–Ernzerhof-GGA (PBE-GGA) is very widely used (Corbett et al., 2017; Ruvalcaba et al., 2021; Maldonado-Lopez et al., 2021) because it gives

consistent results with experimental data. However, there are still some adjustments to the standard DFT needed to model these systems correctly.

2.9 Spin-Dependent DFT

Up to this point, DFT has been discussed in terms of electron density as the fundamental variable. This is the original formulation of DFT, but it is not the most complete nor even the most widely used DFT in practical applications. For instance, spin-polarization is crucial for the modeling of spin probes in organic radicals in biomolecules (Jeschke and Polyhach, 2007), magnetic materials, and spintronic devices (Herrmann et al., 2010). All of these systems require the Spin-Polarized-DFT (SP-DFT) formulation, that employs one density for each spin — $\rho_{\uparrow}(\boldsymbol{r})$ and $\rho_{\downarrow}(\boldsymbol{r})$ — *i.e.*, works with two fundamental variables. These are used to define the total electron density of the system as a linear combination of the two of them (Jacob and Reiher, 2012):

$$\begin{aligned}\rho(\boldsymbol{r}) &= N\int\cdots\int\left|\Psi\left(\boldsymbol{r_1},+\frac{1}{2},\cdots,\boldsymbol{r_N},s_N\right)\right|^2 d\boldsymbol{r_2}ds_2\cdots d\boldsymbol{r_N}ds_N \\ &+ N\int\cdots\int\left|\Psi\left(\boldsymbol{r_1},-\frac{1}{2},\cdots,\boldsymbol{r_N},s_N\right)\right|^2 d\boldsymbol{r_2}ds_2\cdots d\boldsymbol{r_N}ds_N \\ &= \rho_{\uparrow}(\boldsymbol{r})+\rho_{\downarrow}(\boldsymbol{r})\end{aligned} \tag{18}$$

Similarly, the magnetization density can be defined as the difference between the two spin-polarized densities:

$$\xi(\boldsymbol{r}) = \rho_{\uparrow}(\boldsymbol{r}) - \rho_{\downarrow}(\boldsymbol{r}) \tag{19}$$

Almost the entire further development of the HK theorem and the KS equations can be immediately rephrased for SP-DFT just by attaching a suitable spin index to the densities. There are some exceptions to this rule. For example, the exchange-correlation functional gets "spin-scaled" (Capelle, 2006):

$$\widehat{E}_{XC}^{SP-DFT}\left[\rho_{\uparrow}(\boldsymbol{r}),\rho_{\downarrow}(\boldsymbol{r})\right] = \frac{1}{2}\left(\widehat{E}_{XC}^{DFT}\left[2\rho_{\uparrow}(\boldsymbol{r})\right]+\widehat{E}_{XC}^{DFT}\left[2\rho_{\downarrow}(\boldsymbol{r})\right]\right) \tag{20}$$

It is worth noting that there is no fundamental difference in the calculation of systems with collinear versus noncollinear magnetic moments, even though it is directly related to the spin. All that's needed is the converged wave function after a KS calculation to calculate the magnetic moment ($\boldsymbol{m}(\boldsymbol{r})$) as

follows:

$$\boldsymbol{m}(\boldsymbol{r}) = N \langle \Psi | \beta \widehat{\boldsymbol{\sigma}}^{(4)} | \Psi \rangle \tag{21}$$

where β is one of the parameters that defines the Dirac matrices, and $\widehat{\boldsymbol{\sigma}}^{(4)}$ is a vector containing the Pauli spin matrices σ_x, σ_y, and σ_z (Jacob and Reiher, 2012).

In equation (21) the magnetic moment of the non-interacting reference system does not agree with the true interacting system (Jacob and Reiher, 2012). To calculate those properties we must impose the restriction that either the z-components of the magnetic moment $m_z(\boldsymbol{r})$ or the lengths of the magnetic moment at each point $|\boldsymbol{m}(\boldsymbol{r})|$ must agree between the interacting and non-interacting systems. The former is called a collinear model and the latter a noncollinear model for the magnetic moments. Jacob and Reiher (2012) provide an in-depth discussion of the exact theory regarding SP-DFT. In the present thesis, the spatial components of the coordinates are labeled x, y, z or a, b, c interchangeably.

2.10 Hubbard-U scheme

This is a correction to the KS Hamiltonian commonly added to systems that have atoms with partially filled d or f orbitals, which typically have a strong correlation (Dudarev et al., 1998). The idea behind DFT+U is quite simple: describing the "strongly correlated" electronic states of a system using the Hubbard model — which describes the transition between conducting and insulating systems (Hubbard, 1963) —, whereas the rest of the valence electrons are treated at the level of "standard" DFT functionals (Himmetoglu et al., 2014). In this scheme, the total energy $\widehat{E}_{DFT+U}$ of a system can be written as:

$$\widehat{E}_{DFT+U}[\rho(\boldsymbol{r})] = \widehat{E}_{DFT}[\rho(\boldsymbol{r})] + \widehat{E}_{Hub}[\rho(\boldsymbol{r})] - \widehat{E}_{dc}[\rho(\boldsymbol{r})] \tag{22}$$

where $\widehat{E}_{DFT}$ represents the DFT total energy functional, $\widehat{E}_{Hub}$ is the Hubbard Hamiltonian that models correlated states, and $\widehat{E}_{dc}$ is the "double-counting" term. It is subtracted because the Hubbard term was added explicitly, so the energy contribution of the orbitals included in the DFT functional must be removed in order not to count twice their contributions (Côté, 2008). This scheme was described more than two decades ago by Anisimov et al. (1991) and (Solovyev et al., 1994). A simplified explicit expression for the Hubbard and the double-counting term is:

$$\widehat{E}_{DFT+U}[\rho(\boldsymbol{r})] = \widehat{E}_{DFT}[\rho(\boldsymbol{r})] + \frac{U}{2}\sum_{i\neq j}\widehat{n}_i\widehat{n}_j - \frac{U}{2}\left(\sum_i \widehat{n}_i\right)\left(\sum_i \widehat{n}_i - 1\right) \tag{23}$$

where $\widehat{n}_i$ is the number operator of the electron at site i and U is a manually-defined parameter. Equation (23) is only defined for an orthonormal single-particle basis with localized orbitals, representing the strongly correlated electrons (Anisimov et al., 1991).

2.11 Electron Localization Function

The Electron Localization Function (ELF) is a quantum chemistry tool created by Becke and Edgecombe (1990) to help determine the nature of the bonding present at different molecules. This is especially important because, although the electron density is easily obtained via DFT calculations, by itself it does not easily reveal the consequences of the Pauli exclusion principle on the bonding (Silvi and Savin, 1994). In simple terms, the electron density represents the probability density of finding an electron in space, while the ELF measures the probability of finding *another* electron with the same spin near that reference electron (Koumpouras and Larsson, 2020). For DFT, the general expression was given by Silvi and Savin (1994):

$$ELF = \frac{1}{1 + \left(\frac{D}{D_h}\right)^2} \tag{24}$$

with

$$D = \frac{1}{2}\sum_i \left|\boldsymbol{\nabla}\psi_i\left(\boldsymbol{r}\right)\right|^2 - \frac{1}{8}\frac{\left|\boldsymbol{\nabla}\rho\left(\boldsymbol{r}\right)\right|^2}{\rho\left(\boldsymbol{r}\right)} \tag{25}$$

$$D_h = \frac{3}{10}\left(3\pi^2\right)^{5/3}\rho^{5/3}\left(\boldsymbol{r}\right) \tag{26}$$

The ELF has values between 0 and 1, where 1 corresponds to perfect localization — such as in lone pairs or covalent bonds. Koumpouras and Larsson (2020) report that the ELF in metallic bonds has regions with a non-nuclear maxima, with values always lower than 0.7, and with big and extended basins of uniform localization connecting the atoms of the crystal.

2.12 Electrostatic Potential Isosurface

The electrostatic potential of any system can be represented in maps that illustrate the charge distributions of the atoms. They are most commonly used in quantum chemistry to predict the behavior of molecules because they allow to visualize variably charged regions of a molecule (Bottyan, 2020), although they obviously can provide useful information for other types of systems. They are most commonly represented in 2D cuts of the system or as isosurfaces. The former is called an Electrostatic

Potential Isosurface (EPI), which by definition represents all the points in space with equal values of electrostatic potential.

In DFT calculations, the way these are created is by generating isosurfaces of the electronic density of your system and then coloring the surface with the electrostatic potential, which is given by all the non-kinetic terms of the KS-Hamiltonian (Kresse and Furthmüller, 2022c):

$$\widehat{V}_{POT}\left[\rho\left(\boldsymbol{r}\right)\right] = \int \rho\left(\boldsymbol{r}\right) V_{ext}\left[\rho\left(\boldsymbol{r}\right)\right] d\boldsymbol{r} + \frac{1}{2}\int\int \frac{\rho\left(\boldsymbol{r}\right)\rho\left(\boldsymbol{r'}\right)}{\left|\boldsymbol{r}-\boldsymbol{r'}\right|} d\boldsymbol{r} d\boldsymbol{r'} + \widehat{E}_{XC}\left[\rho\left(\boldsymbol{r}\right)\right] \tag{27}$$

Chapter 3. Methodology

3.1 Computational details

The calculations were performed using the Projector Augmented Wave (Blöchl, 1994; Kresse and Joubert, 1999) implementation of DFT in the Vienna Ab initio Simulation Package (VASP) (Kresse and Furthmüller, 1996) version 5.4.4. The exchange-correlation energy was described with the PBE-GGA functional (Perdew et al., 1996). The Mn, Ga, C, and Cu atoms were all represented by ultrasoft pseudopotentials (Vanderbilt, 1990). Structural optimizations were performed using the conjugate gradient method until the net force on every atom was smaller than $0.001\ eV/$Å and the total energies between two steps were different by no more than $10^{-4}\ eV$. The Brillouin zone integrations were performed using a Monkhorst-Pack (Monkhorst and Pack, 1976) k-point grid and a Methfessel-Paxton smearing (Methfessel and Paxton, 1989) of the second-order of the Fermi–Dirac distribution function. The cutoff energies for the plane-wave basis were set to 300, 400, and $550\ eV$ for the α-Mn, D0$_{22}$-Mn$_3$Ga, and L1$_0$-MnGa, respectively. The k-point densities used were $4 \times 4 \times 4$, $10 \times 10 \times 10$, and $8 \times 8 \times 8$ for the α-Mn, D0$_{22}$-Mn$_3$Ga, and L1$_0$-MnGa bulks, respectively. On the supercells, k-point densities used were $4 \times 4 \times 1$, $5 \times 5 \times 1$, and $4 \times 8 \times 1$ for the α-Mn 1×1, D0$_{22}$-Mn$_3$Ga 2×2, and L1$_0$-MnGa 2×1 surfaces, respectively. The surfaces were modeled in a supercell generated by periodically repeating slabs with several atomic planes along the [001] direction and a vacuum larger than 10 Å. The optimized atomic positions were taken for the post-processing calculations, and the k-point densities were tripled. Particularly for the densities of states, the smearing was switched to the tetrahedron method with Blöchl corrections (Blöchl et al., 1994).

On the L1$_0$-MnGa calculations, a DFT+U corrective functional (Dudarev et al., 1998) with an effective on-site Coulomb interaction $U = 5\ eV$ was used on the Mn and Cu atoms to improve the description of electronic correlation and localization. The results obtained using the DFT+U functional were compared with calculations that did not include it (hereby referred to as just DFT calculations). The illustrations of the crystal structures, theoretical STM images, and graphical plots presented in this thesis were generated using VESTA (Momma and Izumi, 2011), Critic2 (de la Roza et al., 2014), and Matplotlib (Hunter, 2007) softwares, respectively. The STM images were simulated using the incorporation of the Tersoff-Hamann theory (Tersoff and Hamann, 1985) to DFT.

3.2 Bulk calculations

Following the order of the objectives presented in **Section 1.4** and the standard methodology for the DFT simulations, firstly the unit cells were generated (as showcased in **Figures 3(b), 2(b), 2(c)**) based on the data files reported in Materials Project (2013a,b,d). Then, an optimization of the internal parameters of the calculations — cutoff energy for the plane-wave-basis set and k-point density — was performed. The final step was a structural relaxation and optimization of the lattice parameter in the bulks. This combination of parameters was used throughout the rest of the calculations, except for the k-point density, which is rounded to the closest even number after dividing it by the multiplicity of the supercell to increase computational efficiency. All the possible magnetic configurations were tested on each Mn-Ga alloy, and their stability was determined. α-Mn is the only structure that was simulated with non-collinear magnetic moments. The other Mn-Ga alloys were simulated only collinearly. Finally, with the energies obtained from these calculations, the enthalpy of formation was calculated, which was later applied in the SFE formalism (see **Annex 1**).

3.3 Surface relaxations

The surface models were defined in supercells based on the unit cells of the bulks. For example, to generate a $n \times m$-model one must repeat the unit cell n times in the a direction, m times in the b direction, then as many times in the c dimension (which matches the $[001]$ direction) as to obtain the desired number of atomic layers, and then provided with a portion of empty space. This vacuum must be greater than 10 Å so as to prevent Van deer Waals interactions due to the periodic boundary conditions (Ruvalcaba et al., 2021; Maldonado-Lopez et al., 2021).

3.3.1 α-Mn

The α-Mn supercells were generated by repeating the optimized bulk two times in the c dimension and adding a vacuum of 10.15 Å. Afterwards, the atomic layers were numbered as shown in **Figure 4(a)**. Because the α-Mn structure is a BCC structure, it has inversion symmetry, which is reflected in labeling the bottom half of the atoms in the unit cell as negative numbers. The atoms' position in negative layers corresponds to a $90°$ rotation in the ab-plane around the center of the cell. The unreconstructed models have the same atomic positions as in the bulk (before the surface relaxation) but with the corresponding

layer number at the surface, and reconstructed models have atom vacancies at the surface according to the number of atoms in their corresponding layer.

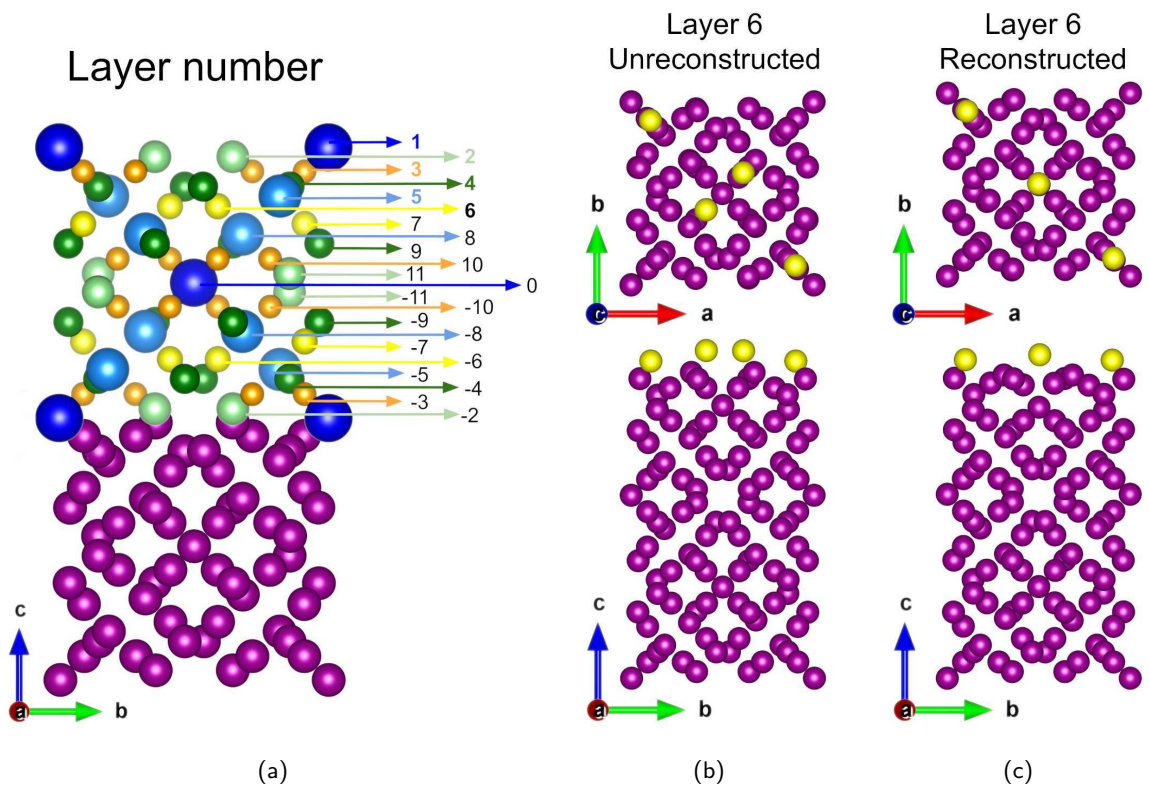

Figure 4. Front and top views of some α-Mn surfaces. (a) Shows the layer numeration. The relaxed structures of the most stable reconstructions are shown in (b) unreconstructed and (c) reconstructed models in layer 6. The atoms in purple represent Mn atoms in general and the rest of the atoms follow the same coloring system as **Figure 1**.

Layer 1 only has one atom, so adding an atomic vacancy equals having the layer-2-unreconstructed model. Therefore, layers 1 and 0 do not have a first-layer reconstructed model. Layer 2 has two atoms, so creating an atomic vacancy leads to two possible surface reconstructions, one for each position of the MnIIIa. However, both positions are magneto-crystallographically equivalent, so only one model was necessary to be simulated. All the possible permutations of one, two, and three vacancies were modeled on layers with four atoms. All the unreconstructed models and their most stable reconstructions are shown in **Figure 19** in **Annex 2**. Since the surface calculations were performed on the CL-AFM ordering, it can be observed in **Figure 3(a)** that atoms in layers of the same sign and color — layers 2 and 11, layers 3 and 10, layers 4 and 9, layers 5 and 8, and layers 6 and 7 (likewise for the negative numbers) — have their magnetic moments oriented in opposite directions. Because of this and the 90° rotation in the ab-plane around the center of the cell, it was determined that all the negative layers will yield the same surface patterns but rotated 90°. Therefore, only layers 0–11 were simulated. **Figures 4(b),4(c)** show

the final relaxed structure of the two models in layer 6. All of these models were generated looking for the atomic arrangements that explained the experimentally observed row- and square- reconstructions shown in **Figure 8**.

3.3.2 D0$_{22}$-Mn$_3$Ga

The D0$_{22}$-Mn$_3$Ga supercells were generated by repeating the optimized bulk 2.5 times in the c dimension and then adding a vacuum of 11.81 Å. This process generated the Mn$_y$-Ga-terminated model B (**Figure 5(b)**) and by taking the last atomic layer off, a Mn$_x$-Mn$_x$-terminated model A (**Figure 5(a)**) was created.

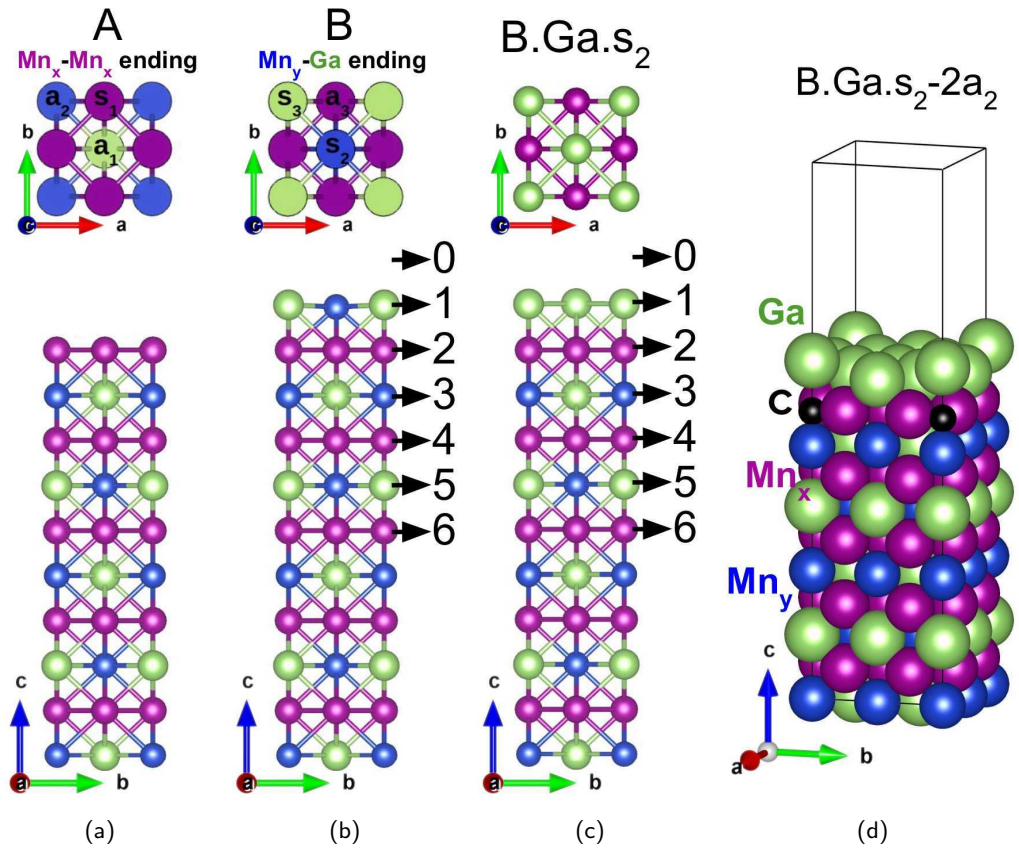

Figure 5. Different views of the some surface reconstructions of D0$_{22}$-Mn$_3$Ga. The base reconstructions are (a) model A and (b) model B. Surface nomenclatures adopted for the adsorption (sites a$_{1,2,3}$) and substitution (s$_{1,2}$) sites are shown. Model (c) B.Ga.s$_2$ is based on model B and has a Ga atom substituted in position s_2. Figures (b) and (c) also show the number assigned to each layer. Model (d) B.Ga.s$_2$-2a$_2$ models a C incorporation in the second layer. The purple, dark blue, turquoise, and black colors represent the Mn$_x$, Mn$_y$, Ga, and C atoms, respectively.

The nomenclature for these surface reconstructions goes as follows: (model on which it is based).(metal added).(position of adsorption/substitution). Therefore, model B.Ga.s$_2$ is based on model B and has a

Ga atom substituted in position s_2. The rest of the surface models are shown in **Figure 20** in **Annex 2**. Once the most stable surface reconstructions were determined, the C diffusion was evaluated in 2×2 supercells such as the B.Ga.s$_2$-2a$_2$, which is based on model B.Ga.s_2 but with a C atom adsorbed in layer 2 in position a_2 (see **Figure 5(d)**). These larger supercells allowed to model also the properties of the D0$_{22}$-Mn$_3$Ga with a 1.12 % C layer-uniform doping. Doping ranging from 0.06–1.18 % was previously studied experimentally and theoretically by Gutiérrez-Pérez et al. (2017); Holguín-Momaca et al. (2019), but only focusing on the properties of the material in bulk.

3.3.3 L1$_0$-MnGa

The L1$_0$-MnGa supercells in **Figure 6** were generated by repeating the optimized bulk 4 times in the c dimension and then adding a vacuum of 16.62 Å. The models were simulated using DFT, and then the most stable ones were also simulated using DFT+U.

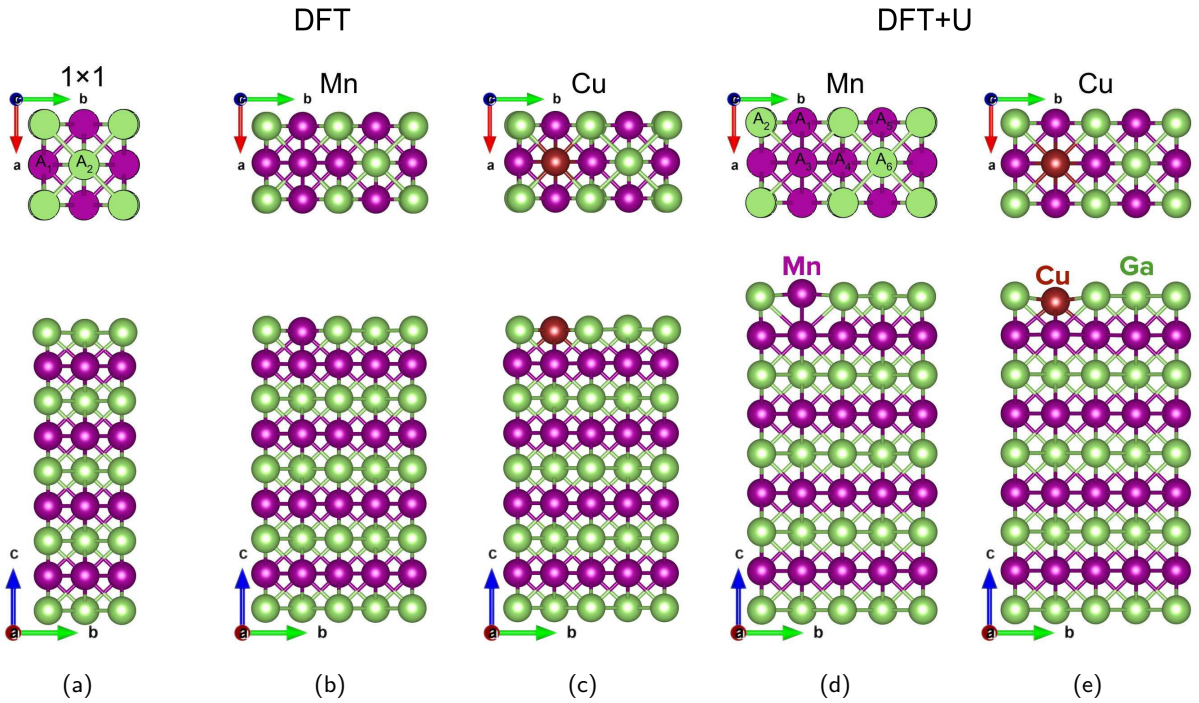

Figure 6. Front and top views of the (a) 1×1 and most stable surfaces of L1$_0$-MnGa calculated on both (a,b,c) DFT and (d,e) DFT+U frameworks. Positions for the adsorption in both the 1×1 (sites A$_{1,2}$) and 2×1 (sites A$_{1,2,3,4,5,6}$) reconstructions are shown in (a) and (d), respectively. Models labeled "Mn" are equivalent to the 1×2 reconstruction reported in Corbett et al. (2017) and models labeled "Cu" are equivalent to model Cu/Mn$_1$(S$_1$) in **Section 4.3**. The purple, turquoise, and brown colors represent the Mn, Ga and Cu atoms, respectively.

The 1×1 (see **Figure 6(a)**) and Mn (see **Figures 6(b), 6(d)**) surface models were based on the study of Corbett et al. (2017). A more detailed explanation on the definition of all the models can be found

in **Section 4.3.1**. The names of the 1×2 models in **Figure 6** are given by the substituted atom at the surface layer and the rest of the modeled surface reconstructions are shown in **Figure 21** in **Annex 2**.

3.4 Surface stability and post-processing

Once the surface models were all defined and calculated, the next step was to determine their stability. The total energy of the systems cannot be compared because the number of atoms of each element varied for each reconstruction. In this instance, the SFE formalism was adapted from the article of Qian et al. (1988) to determine the stability of the different reconstructions and determine the most stable in each alloy. A more detailed development of this formalism is shown in **Annex 1**.

Finally, once all of the wave functions of the most stable reconstructions are calculated, they are further studied in a stage known as post-processing. This consisted of shorter calculations to obtain the properties of interest of the surfaces (see **Chapter 4**). The theoretical STM images (TH-STM) of the most stable reconstructions for α-Mn and L1_0-MnGa were obtained. The simulations were done by positioning the tip at distances between 3 and 4 Å with the same bias voltage used in the experimental analyses. The magnetic properties of the alloys were also calculated — such as the direction of the magnetic moments on the surface of α-Mn or the magnetic moments per atom in the more stable surfaces of D0_{22}-Mn_3Ga and L1_0-MnGa — the latter being compared with their bulk counterparts. The Projected Densities Of States (PDOS) of D0_{22}-Mn_3Ga and L1_0-MnGa were calculated. On the L1_0-MnGa a more profound study was performed. The ELF was calculated, as well as the magnetization density and the EPI.

Chapter 4. Results and Discussions

4.1 α-Mn

Firstly the results of the calculations on the bulk cells are presented. **Figure 7(a)** shows the energy versus unit cell volume graph of the α-Mn structure. Only the NM, the CL-AFM, and the NCL-AFM orders reached stability in this alloy. The FM configuration was tested, but the magnetic moments quickly returned to an AFM order. It is clear that α-Mn's NM structure is less stable than any of the AFM ones. The optimal cell volume varies with the magnetic order due to variations in the atoms' internal forces caused by their magnetic interactions. Within the chosen framework, the most stable configuration is a CL-AFM with a unit cell volume of 11.21 $Å^3$/atom, which equals to the lattice parameters $a = b = c = 8.66$ Å. This value matches the experimental result of 8.894 Å from Bradley and Thewlis (1927) with an error of 2.63 %. The ground state energy of α-Mn is -524.72 $eV/cell$, with a difference of 2.86 $eV/cell$ with the NM configuration.

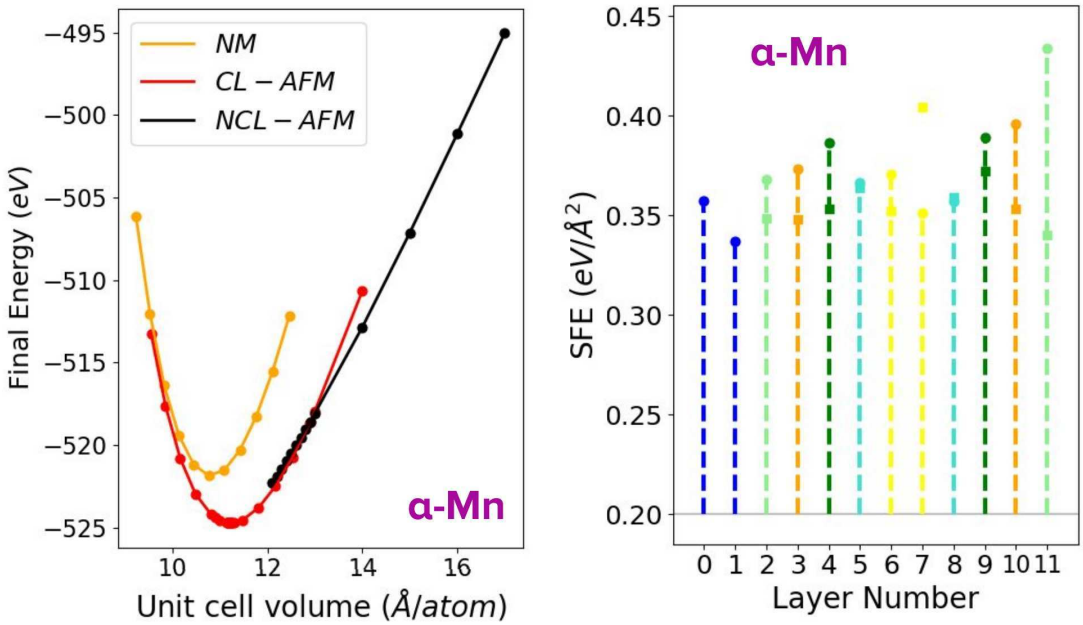

(a) (b)

Figure 7. Stabilities of the α-Mn bulk (in all of its possible magnetic orders) and surface reconstructions: (a) Final energy vs. unit cell volume graph and (b) Surface Formation Energy graph. Circles represent the unreconstructed models and squares represent the most stable reconstructed models.

According to **Figure 7(a)** the α-Mn structure behaves interestingly under strain: it is a CL-AFM under compressing strain, at its ground state, and up until a stretching strain of 2.30 %. Then as the cell

gets further stretched, the magnetic symmetry is broken, and the magnetic moments shift to a NCL configuration. The shifting of the magnetic moments is given at 12.1 Å$^3/atom$ ($a = b = c = 8.89$ Å), almost exactly the experimental value (Lawson et al., 1994). This value does not stray far from the 12.0 Å$^3/atom$ value reported by Hobbs et al. (2003) for the same behavior. However, the surface calculations were performed with the CL-AFM structure since it is the ground state within the chosen framework. That said, the present results may be tested with experimental studies on the α-Mn surfaces to verify their exactitude or show the need for further corrections on the DFT description.

Table 1. Calculated atomic positions and magnetic moments of the optimal and the NCL-AFM bulks of α-Mn.

Atom type	Number	Crystal coordinates
MnI	2	$(0,0,0)\,,\left(\frac{1}{2},\frac{1}{2},\frac{1}{2}\right)$
MnII	8	$[(x,x,x)\,,(x,-x,-x)\,,(-x,x,-x)\,,(-x,-x,x)]$ $+\left[(0,0,0)\,;\left(\frac{1}{2},\frac{1}{2},\frac{1}{2}\right)\right],\ x(\text{II})=0.319$
MnIIIa	8	$[(x,x,z)\,,(x,-x,-z)\,,(-x,x,-z)\,,(-x,-x,z)]$ $+\left[(0,0,0)\,;\left(\frac{1}{2},\frac{1}{2},\frac{1}{2}\right)\right],x(\text{IIIa})=0.356,\ z(\text{IIIa})=0.035$
MnIIIb	16	$[(x,y,x)\,,(x,-y,-x)\,,(-x,y,-x)\,,(-x,-y,x)\,,(y,x,x)\,,$ $(y,-x,-x)\,,(-y,x,-x)\,,(-y,-x,x)+\left[(0,0,0)\,;\left(\frac{1}{2},\frac{1}{2},\frac{1}{2}\right)\right],$ $x(\text{IIIb})=0.356,\ y(\text{IIIb})=0.035$
MnIVa	8	$[(x,x,z)\,,(x,-x,-z)\,,(-x,x,-z)\,,(-x,-x,z)]$ $+\left[(0,0,0)\,;\left(\frac{1}{2},\frac{1}{2},\frac{1}{2}\right)\right],\ x(\text{IVa})=0.089,\ z(\text{IVa})=0.283$
MnIVb	16	$[(x,y,x)\,,(x,-y,-x)\,,(-x,y,-x)\,,(-x,-y,x)\,,(y,x,x)\,,$ $(y,-x,-x)\,,(-y,x,-x)\,,(-y,-x,x)+\left[(0,0,0)\,;\left(\frac{1}{2},\frac{1}{2},\frac{1}{2}\right)\right],$ $x(\text{IVb})=0.089,\ y(\text{IVb})=0.283$

Atom type		$\lvert m_z\rvert$ (μ_B)		$\lvert m_x\rvert$ (μ_B)	$\lvert m_y\rvert$ (μ_B)	$\lvert m_z\rvert$ (μ_B)
MnI		2.94		0.00	0.00	3.23
MnII		2.38		0.02	0.02	2.83
MnIIIa	CL-AFM	1.34	NCL-AFM	0.45	0.44	1.82
MnIIIb1	11.21	1.35	12.1	0.04	0.45	1.88
MnIIIb2	Å$^3/cell$	1.35	Å$^3/cell$	0.45	0.04	1.88
MnIVa		0.02		0.53	0.52	0.02
MnIVb1		0.03		0.54	0.01	0.01
MnIVb2		0.03		0.01	0.54	0.01

Table 1 gives the positions and magnetic moments of the α-Mn structures. Only the magnitudes of the magnetic moments are given, and the direction can be obtained by looking at **Figure 3(b)**. On the NCL-AFM structure, the MnIIIb and MnIVb atoms can be further categorized into the two subgroups

b1 and b2. This was also proposed by Yamagata and Asayama (1972) based on their nuclear magnetic resonance data and by Hobbs et al. (2003) in their theoretical study. The magnetic moments of the atoms in these two subgroups only differ in orientation, as they have almost the same magnitude.

4.1.1 Surface stability analysis

The SFE formalism was applied to all the simulated models. As mentioned in the previous chapter, only layers 0–11 of the top cell in the supercell were simulated since all of the other layers would yield the same patterns but rotated 90°. **Figure 7(b)** shows the SFE graphs of the models. Models based on layers 3, 4, 9, and 10 only are presented with their most stable reconstruction since they have four atoms in their corresponding layer and have a total of 5 different reconstructions. It is clear that the unreconstructed-layer-1 model has the smallest SFE (0.337 $eV/$Å^2), hinting that it is the most stable one and the most likely to be present experimentally. However, as mentioned before, layer-1 and layer-0 models do not possess a first-layer reconstruction. Therefore they cannot yield the two different reconstructions that are being searched. Also, it is worth noting that the SFE formalism points at the model that is most easily synthesized. Any other model could be induced experimentally with an extra input of energy via any method that allows controlling the stoichiometry of each atomic layer — such as Chemical Vapor Deposition, Atomic Layer Deposition, or Molecular Beam Epitaxy (Xu et al., 2022).

Now, our collaborator, Dr. Perry Corbett, reported that both surface terminations appear on the same atomic terrace (see **Figure 8**(a)). So, another criterion was if the theoretical STM images generated by the models of each layer could generate both the row- and square- reconstructions. As it turns out, only layers 6, 8, and 10 generate both square- and row- reconstructions, and among these three, the most stable one is layer 6, with its lowest SFE value at 0.352 $eV/$Å^2, against 0.357 and 0.353 $eV/$Å^2 for layers 8 and 10, respectively. However, the difference in formation energies is quite small. A Fourier analysis of the theoretical STM images was performed on these three layers and compared with experimental images to further determine the model with the greatest match to the experiment, which leads us to the next section.

4.1.2 Structural and STM analysis

Figure 8 shows the comparison of theoretical and experimental STM images of the two models in layer 6 in real and reciprocal space. **Figure 8(a)** shows the experimental STM image portraying the two analyzed

reconstructions: the 1×1 square-reconstruction and the row-reconstruction. Our Dr. Corbett reports that a third large-row-vacancy-reconstruction is present (not shown herein), that all three terminations can appear on the same atomic terrace, and that when they do not, they are rotated $90°$. The first of these three statements is sadly out of the scope of this work, but there certainly is something we can do about the last two. Given our model for the α-Mn surface reconstructions, the rotated zones belong to layer -7 and have a height difference of an integer multiple of $c/2$. This means that in a single terrace, the different structures can grow from the same underneath layer, as displayed by Wulfhekel and Gao (2010).

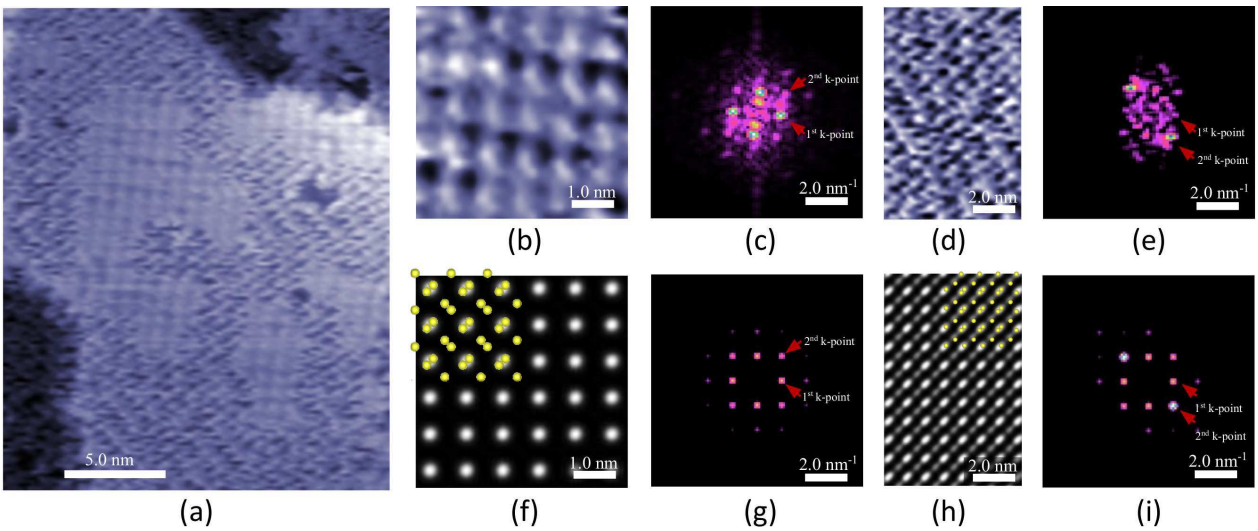

Figure 8. Experimental and theoretical STM images of the α-Mn surface. (a) Experimental STM image showing the two reconstructions. Atomic contrast was enhanced by Laplacian filtering. Image also includes zoomed views of the experimental (b) square- and (d) row- structures, as well as theoretical TH-STM images of (f) unreconstructed-layer-6 model showing a square-structure and (h) reconstructed-layer-6 model showing a row-structure ($V = -0.5V$, $d = 4$ Å). Images (c,e,g,i) display the Fast Fourier Transforms of the experimental and theoretical STM images in (b,d,f,h), respectively. Experimental and FFT images were provided by collaborator Dr. Perry Corbett.

By analyzing the experimental **Figures 8(b,d)** it is estimated that there is a separation of 8.6 ± 0.5 Å between each point in the square-reconstruction and 6.4 ± 0.5 Å between each row in the row-reconstruction. The theoretical TH-STM images obtained are almost identical in appearance to the experimental images. The estimated distances for the theoretical square- and row- reconstructions are 8.66 Å and 6.12 Å, respectively, well inside the standard deviation. The unreconstructed-layer-6 model generates a square-pattern and the reconstructed-layer-6 model generates the row-pattern, as shown in **Figures 8(f,h)**. In the square-reconstruction (**Figure 8(f)**) each contiguous pair of atoms generates a high-contrast zone at the selected bias and distance. It is worth noting that layers 6 and 7 are located at almost the same height after the surface relaxation. In the row-reconstruction (**Figure 8(h)**), the high-contrast areas are generated by the pair of atoms in layer 7, whilst the lone atom in layer 6 generates

the lower-contrast region in between them.

Now, by comparing the Fast Fourier Transforms (FFTs) of all unreconstructed layers to the experimental FFT, the unreconstructed-layer-6 model best fits both the square- and row- lattices. The fit is based on the arrangement and intensity of the first- and second-order k-points (see **Figures 8(c,g)**). The first-order k-points are of equal intensity in a square array, followed by a rotated square lattice of equal intensity second-order k-points. The FFTs of layers 8 and 10 contained unequal intensity first- and second-order k-points, which did not match the experiment. Also, the reconstructed-layer-6 model is the only one to have a FFT with pair of high-intensity second-order points corresponding to the row structure. Additionally, weaker first- and second-order k-points forming a square are observed in both experiment and theory (see **Figures 8(e,i)**). This gives the best match for coexistence on a single layer, correctly modeling the experimental observations.

4.1.3 Magnetic properties analysis

At the surface there is a breaking of the symmetry of the crystal structure. This leads to the creation of dangling bonds and the relaxation of the atomic positions. These factors create a surface effect that influences the electronic and magnetic properties of the atoms close to the surface. A prime example of this is shown in **Figure 9**, where a NCL behavior of the magnetic moments is presented at the surface layers.

The magnetic moments in the unreconstructed-layer-6 model present canting at the surface. The net magnetic moment of the supercell is $\boldsymbol{m} = (1.546, -0.015, 0.506)\,\mu_B$, as opposed to the zero-value of the bulk. However, as one may observe on **Figures 9(a,b)**, every atom at the surface has its pair with an opposite component in the ab-plane. The value of $m_x = 1.546$ is mainly due to the atom at the bottom of the supercell. This atom should have its magnetic moment collinear such as in the bulk, but instead got projected onto the ab-plane. This does not affect the behavior of the magnetic moments at the surface and got caused because of the surface effect of the vacuum on the bottom of the cell due to the imposed symmetry of the calculations. There is a net value in the c-component of $\boldsymbol{m}$ because of the way the supercells were defined. There is a complete unit cell at the bottom, and then another one with atomic layers 1–5 removed. With this unit cell on top incomplete, there is a net magnetic component in the c-direction.

On flip side, the magnetic moments in the reconstructed-layer-6 model (see **Figures 9(c,d)**) present a

complete projection of the magnetic moments onto the surface plane. The net magnetic moment of the supercell is $\boldsymbol{m} = (1.676, -1.676, -2.124)\,\mu_B$. Again, the magnetic component in the c-axis is due to how the supercells were described. The lone atom in layer 6 causes the net magnetic moment in the ab-plane since it is the only atom that does not possess a partner to cancel out with. Interestingly enough, the spin distribution map reported by Wulfhekel and Gao (2010) strongly resembles the pattern shown at both surfaces, with magnetic moments oriented diagonally along the unit cell.

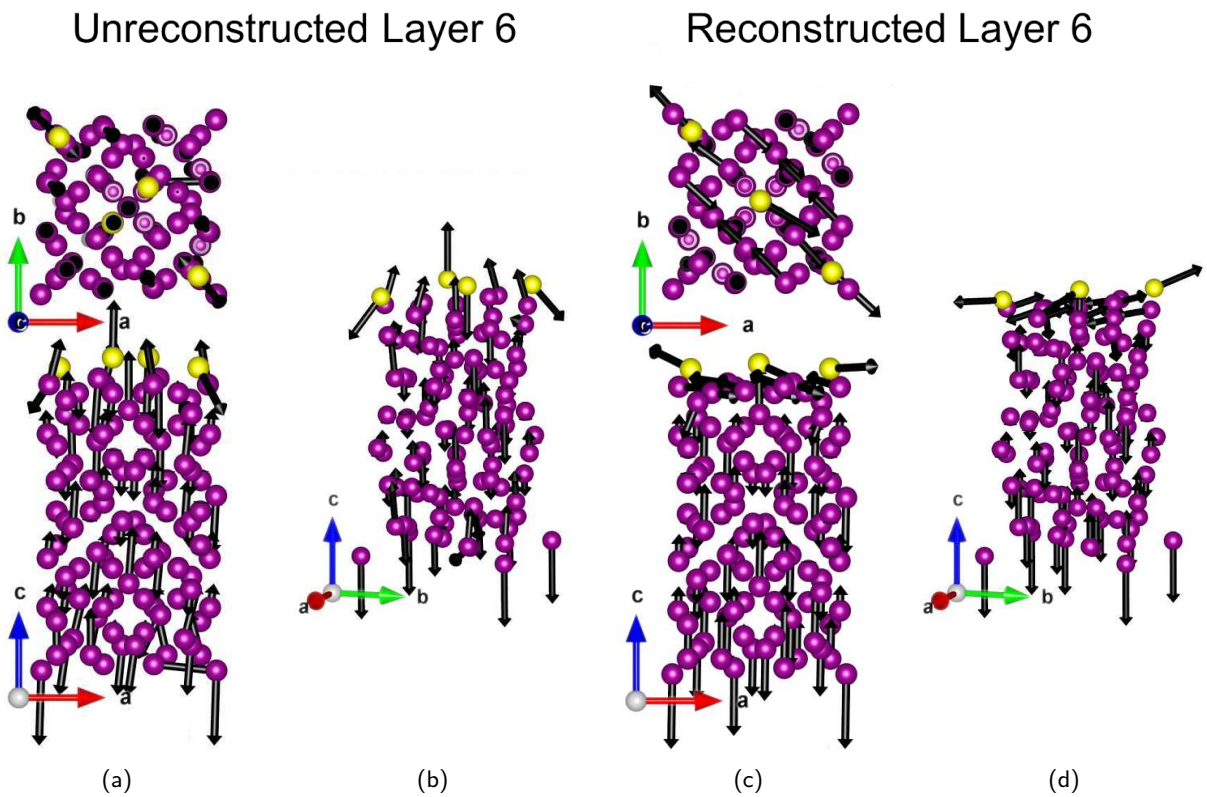

Figure 9. Graphical representation of the magnetic moments per layer of the (a) top and front and (b) isometric views of the unreconstructed-layer-6 model and the the (c) top and front and (d) isometric views of the reconstructed-layer-6 model of the α-Mn.

4.2 D0$_{22}$-Mn$_3$Ga

As for D0$_{22}$-Mn$_3$Ga, **Figure 10(a)** shows that more magnetic configurations were possible for this structure, mainly because of the crystal symmetry of the unit cell. In both this and the L1$_0$-MnGa structures, all magnetic orders were collinear as no report exists of these structures displaying a non-collinear behavior. Therefore the prefixes CL- and NCL- are dropped henceforth. This structure shows a fM ground state with the magnetic moments of Mn$_x$ atoms coupling in the opposite direction to the ones of the Mn$_y$ atoms (see **Figure 2(b)**). The final energy of this configuration is $-60.52\ eV/cell$. The FM, AFM, and NM structures are less stable by 0.78 $eV/cell$, 0.87 $eV/cell$, and 1.84 $eV/cell$,

respectively.

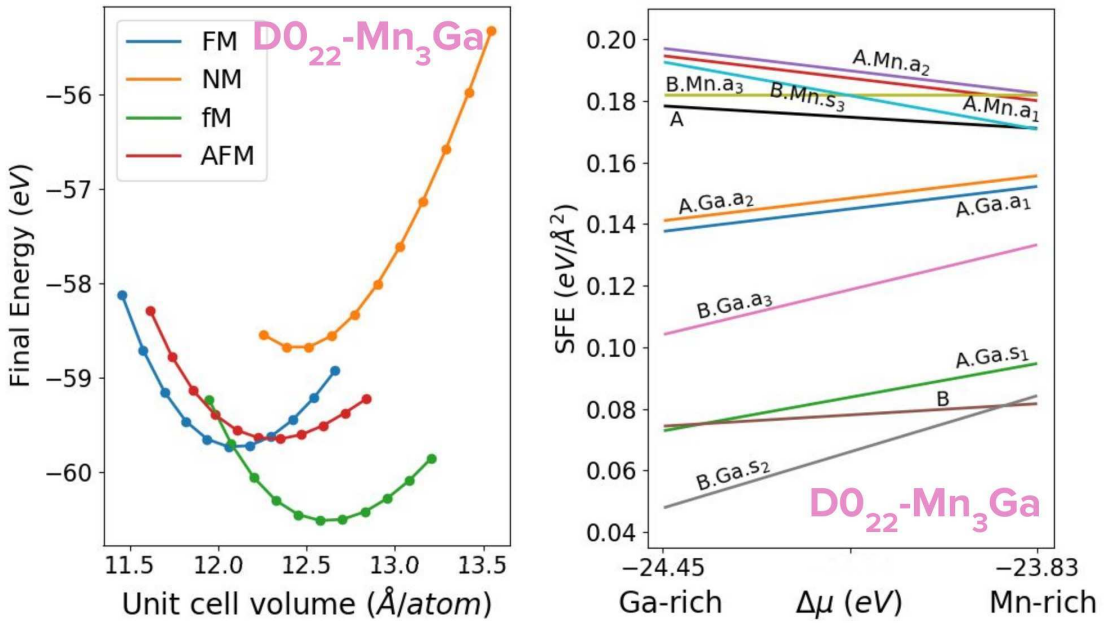

(a) (b)

Figure 10. Stabilities of the D0$_{22}$-Mn$_3$Ga bulk (in all of its possible magnetic orders) and surface reconstructions: (a) Final energy vs. unit cell volume graph and (b) Surface Formation Energy graph.

The magnetic moments of the Mn atoms in the FM configuration are all pointing in the same direction, and in the NM configuration, their magnitude is zero. In the AFM structure, the magnetic moments of the Mn atoms of the top half of the cell are pointing in the opposite direction as the bottom half to cancel out in total. It is worth mentioning that the Ga atoms do not significantly contribute to the magnetism of the structure. The fM structure possesses a unit cell volume of 12.58 Å^3/atom, with respective lattice parameters $a = b = 3.77$ Å and $c = 7.10$ Å; which are well within an error of 3.5 % with other theoretical (Balke et al., 2007) — $a = b = 3.77$ Å and $c = 7.16$ Å — and experimental (Krén and Kádár, 1970) — $a = b = 3.90$ Å and $c = 7.12$ Å — reports. The magnetic moments of the atoms calculated for this magnetic configuration are: $m_{Mn_x} = 2.30\mu_B$, $m_{Mn_y} = -2.82\ \mu_B$, and $m_{Ga} = -0.06\ \mu_B$, which result in a total magnetization of $3.45\ \mu_B/unit\ cell$. These values match almost perfectly the theoretical results of Balke et al. (2007): $m_{Mn_x}, m_{Mn_y} = 2.36, -2.90\ \mu_B$. The same holds for the experimental report, except for the m_{Mn_x}, which Krén and Kádár (1970); Niida et al. (1996) reported to be around $1.6 \pm 0.3\ \mu_B$. This discrepancy affects the numerical value of the magnetic moment, but not its behavior when interacting with the surface or the C, as shall be seen in upcoming sections.

4.2.1 Surface stability analysis

The locations of the Mn_x, Mn_y, and Ga atoms in the unit cell of the $D0_{22}$-Mn_3Ga in fractional coordinates are: $\left[\left(0,\frac{1}{2},\frac{1}{4}\right);\left(\frac{1}{2},0,\frac{1}{4}\right)\right]+\left[(0,0,0);\left(\frac{1}{2},\frac{1}{2},\frac{1}{2}\right)\right]$, $\left[\left(\frac{1}{2},\frac{1}{2},0\right)\right]+\left[(0,0,0);\left(\frac{1}{2},\frac{1}{2},\frac{1}{2}\right)\right]$, and $[(0,0,0)]+\left[(0,0,0);\left(\frac{1}{2},\frac{1}{2},\frac{1}{2}\right)\right]$, respectively. Therefore, the $D0_{22}$-Mn_3Ga structure only has two possible surface terminations: Mn_x-Mn_x and Mn_y-Ga, further referred to as A and B, respectively (see **Figures 5(a,b)**). Zhang et al. (2021) previously studied the stability of these two pristine surfaces via the SFE formalism, but did not consider all the possible first-layer reconstructions. The surface reconstructions were defined based on the adsorption and substitution of atoms on the first layer on surfaces A and B. Surface A has substitution site s_1, in which a Mn_x atom of the first layer can be replaced by a Ga atom. This is model A.Ga.s_1. It also has adsorption sites a_1 and a_2, which are located on top of the Ga and Mn_y atoms of the second layer, respectively. From these sites four models are stemmed: A.Mn.a_1, A.Mn.a_2, A.Ga.a_1, A.Ga.a_2. Similarly, surface B has adsorption site a_3, on top of the Mn_x atom of the corresponding second layer. It also has substitution sites s_2 and s_3, in which either a Mn_y or a Ga atom of the first layer can be replaced by a Ga or Mn_y atom, respectively. All models follow the same nomenclature and are displayed in **Figure 20** in **Annex 2**. Substituted and adsorbed Mn atoms always prefer to keep the spin alignment of their corresponding layer, which is why model names do not differentiate between Mn_x and Mn_y. The only exception to this is the B.Mn.a_3 model, in which the Mn atom adsorbed at the surface is located in a Mn_x-Mn_x layer but couples ferromagnetically to the Mn_y on the surface. This is a surface effect due to the adsorbed Mn atom having no neighbors other than the Mn_y and the Ga atoms at the surface. The Goodenough-Kanamori-Anderson (GKA) rules dictate that a superexchange interaction at 180° along the d–p–d orbitals in an octahedron exhibits a strong AFM coupling, while interaction at 90° is FM (Kanamori, 1959). They also dictate that the expectancy-value of a FM coupling depends on the cosine of half the angle, while the expectancy-value for an AFM depends on the sine of the same argument (Goodenough, 2008). There is a coupling angle of approximately $60°$ bridging of the two magnetic Mn atoms to the non-magnetic Ga, which according to the GKA rules, dictates a FM coupling is more likely. The adsorbed Mn atom in similar reconstructions such as A.Mn.a_1 and A.Mn.a_2 still has an AFM coupling because there is no Ga at the surface, as there must be a non-magnetic anion to carry out the superexchange interaction. **Figure 10(b)** shows the SFE graph of the aforementioned models.

Models A and B show the same behavior and agree with the SFE values reported in the previous study by Zhang et al. (2021). Interestingly, the two most stable surface models stem from a Mn_y-Ga termination: B.Ga.s_2 for Ga-rich conditions and B for Mn-rich conditions. They are the most stable because they have

the lowest SFE values of all the proposed models. The models with a Ga substitution or adsorption follow in stability, which suggests that Ga increases the stability of the reconstructions it is added on. The opposite is true for the reconstructions with either a Mn adsorption of substitution: they are the least stable. This trend has been observed on other Ga-based compounds such as CoGa (Pan et al., 2001), MnGa (Corbett et al., 2017), and Fe_3Ga (Ruvalcaba et al., 2021). Furthermore, model B.Ga.s_2 has a Ga-mono layer termination, and it is the most stable reconstruction on most of the growth conditions.

Now its turn to focus on the adsorption of C atoms on the surfaces of the most stable models (B.Ga.S_2 and B) and their diffusion towards the bulk. The C incorporation was simulated only in interstitial octahedral positions because the ratios of the atomic radius of C ($= 0.70$ Å) to those of Mn ($= 1.40$ Å) and Ga ($= 1.30$ Å) (Slater, 1964) are always less than 0.59, therefore favoring an interstitial alloy (Goldschmidt, 1967, p. 14). Gutiérrez-Pérez et al. (2017); Holguín-Momaca et al. (2019) also found that substitutional positions are unstable. The position of the C atoms relative to the surface was given as follows: each atomic layer was numbered according to their position from the vacuum. Layer 1 is the closest one to the vacuum, and layer 0 is the position of an imaginary layer at the vacuum level to simulate the incorporation of C atoms to the $D0_{22}$-Mn_3Ga structure. Some C atoms were positioned in positions a_1 and a_2, and some others in position a_3, depending on the layer they are located in (see **Figure 5** for graphical representation of these positions). **Figure 11** shows the energies of each C-adsorption model relative to the most stable configuration of each reconstruction (B-6a_2 and B.Ga.s_2-2a_2).

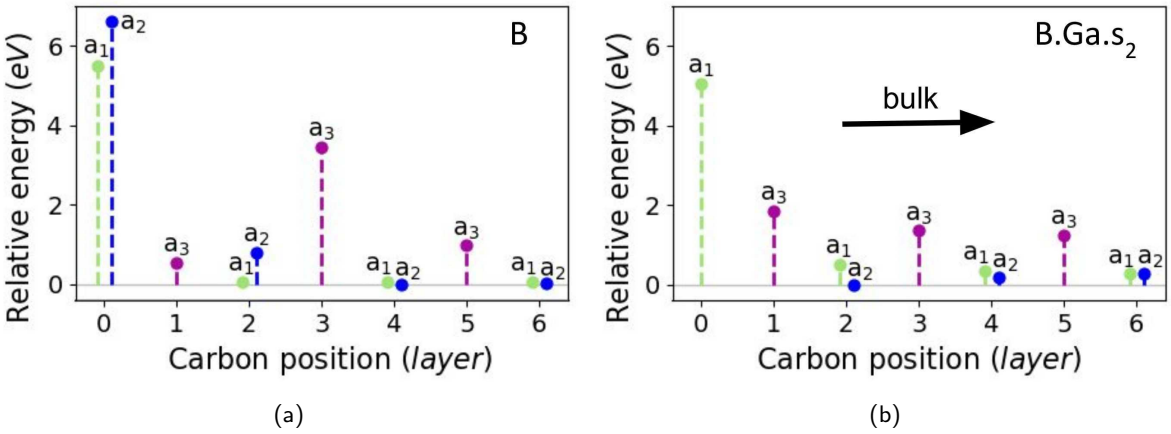

Figure 11. Relative energy vs carbon position graphs of the (a) B and (b) B.Ga.s_2 models. The energy is measured in relation to the most stable adsorption configuration of each model. Adsorption site of each C atom on every layer is labeled next to its corresponding dot. The color represents the type of atom the C atom is laying on.

It is clear that as the C atom diffuses towards the bulk, the structure becomes more stable. The most stable positions for the C atoms are the adsorption sites a_2 in layers 6 and 2 for the B and B.Ga.s_2 reconstructions, respectively. Both of them belong to an even-numbered layer, which is formed by Mn_x

atoms. This is exactly the same result reported by Holguin-Momaca, et al Gutiérrez-Pérez et al. (2017); Holguín-Momaca et al. (2019) when they studied the bulk structure. The least stable adsorption positions are in layer 0, followed by odd-numbered layers; where the C atom just adheres to the atoms at the surface or lies in a Mn_y-Ga layer, respectively (see the side views of **Figure 13** for a graphical representation).

4.2.2 Magnetic properties analysis

As mentioned above, $D0_{22}$-Mn_3Ga is fM, which means that the magnetic moments of Mn_x atoms are aligned in the opposite direction and with a different magnitude than Mn_y and Ga atoms — the latter ones with a minimal contribution. **Figure 12** shows the magnetic moments of each atom in each atomic layer of the two reconstructions from the surface layer (on the left) to the bulk (to the right). The values of the magnetic moments of the Mn_x, Mn_y, and Ga atoms obtained from the calculations in the bulk are included as horizontal lines for comparison. It is worth noting that the C atoms also have a tiny contribution to the total magnetic moment, of approximately $0.03\ \mu_B$. It is also worth recalling that, since the C atoms are adsorbed in octahedral sites of the structure, they are surrounded by 6 atoms at all times — except for when the C is at the surface. These atoms that act as the octahedron's vertices that contain the C atom are represented with a black border.

All the subfigures in **Figure 12** show the surface effect on the magnetic moments. In the models based on the B reconstruction (**Figures 12(a-f)**), the first layer has the magnetic moment of the Mn_y increasing in magnitude to about $-3.3\ \mu_B$ and the Mn_x decreasing in magnitude to about $2\ \mu_B$. The Ga atoms on the surface revert their sign, but their magnitude remains close to zero. This surface phenomenon affects the monolayers closest to the surface and becomes negligible after the second layer. Also, the further the layers are from the surface, the more they will behave like the bulk structure, with the bulk values as an asymptote. The atoms at the bottom layer deviate from the asymptote due to the vacuum being next to them, in a similar manner to what was observed in **Section 4.1.3**.

The behavior of the magnetic moments of Mn atoms is dictated by an interaction between the surface effect, the magnetoelasticity due to the lattice deformation caused by the C, and the superexchange interaction. Gutiérrez-Pérez et al. (2017) proposed that when doping the material, there is a $90°$ superexchange interaction between the d orbitals of the Mn_x and Mn_y atoms and the d orbital of the C, which enhances the magnetization of the material. They also reported a 450 % increment of the total magnetic moment of a bulk doped with 6.25 % C via a DFT calculation compared to experimental

undoped measurements. The total magnetic moments of the 2×2 supercells of undoped models B and B.Ga.s$_2$ were 20.662 and 33.987 μ_B, respectively. The magnetic moments of the doped models were 19.969, 19.000, 18.420, 18.666, 18.678, and 18.946 μ_B for the B models with C in layers 1–6, respectively. For the B.Ga.S$_2$ models with C in layers 1–6 the total magnetic moments were 33.203, 32.367, 34.230, 32.117, 32.529, 32.054 μ_B, respectively. The total magnetic moments of the doped supercells decreased in almost all cases. This apparent contradiction with previous reports is explained by noting that the incorporation of C atoms has a local effect on the magnetic moments.

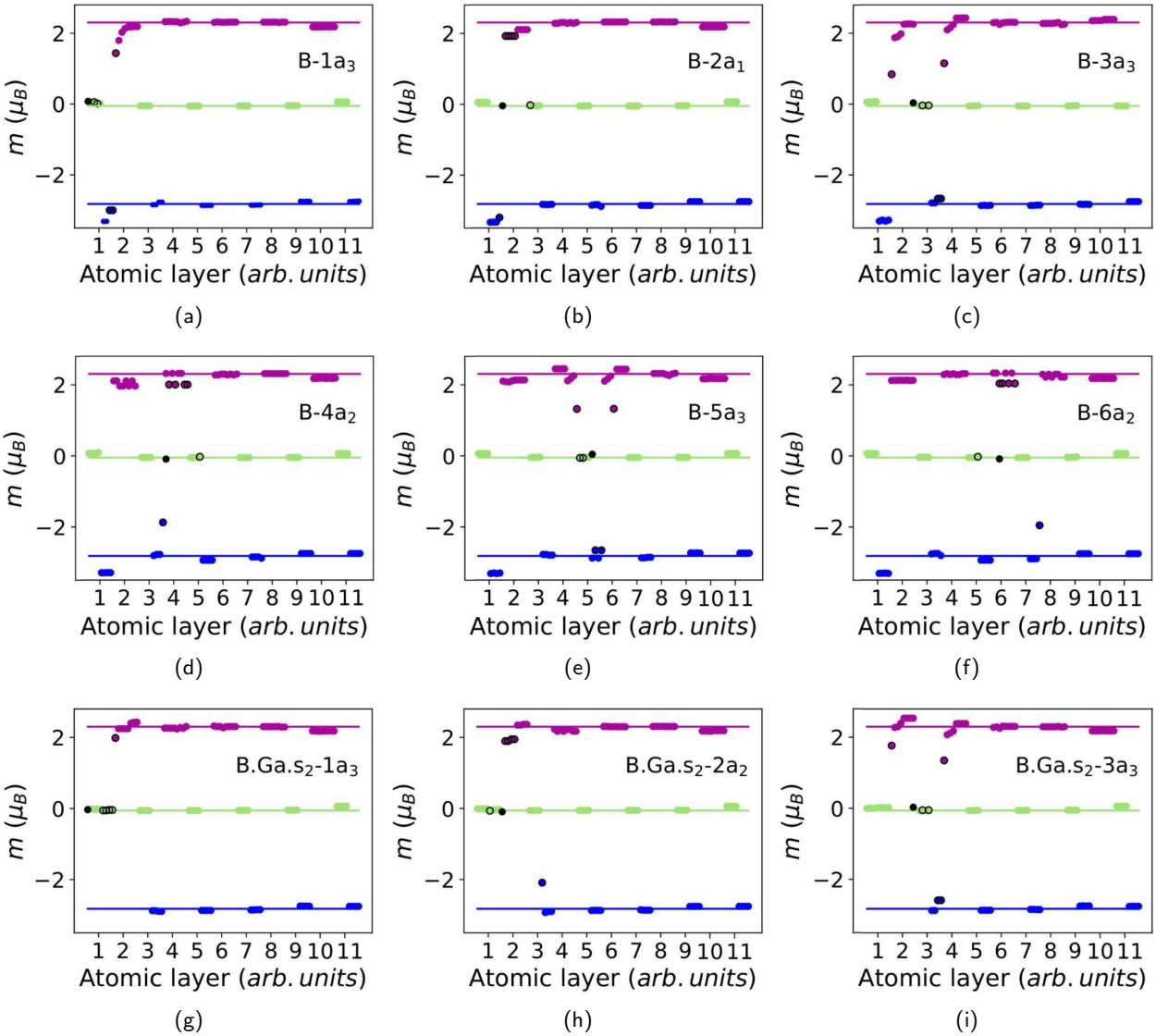

Figure 12. Analysis of the surface magnetic moments per layer of the D0$_{22}$-Mn$_3$Ga. The information of model B with a C atom in the most stable positions in layers (a) 1, (b) 2, (c) 3, (d) 4, (e) 5, and (f) 6; as well as on model B.Ga.s$_2$ in layers (g) 1, (h) 2, and (i) 3 is shown. Dots with a black border represent the first neighbors to the adsorbed C-atom. The rest of the dots follow the coloring system given in **Figure 5**.

The C atom affects differently the magnetic moment of the Mn atoms as it makes its way to the

bulk: it reduces the magnetic moment of the first-neighbor atoms and increases the magnetic moment of the second neighbors. In the surface layers shown in **Figures 12(a,b,g,h)** this effect is almost negligible in comparison to the surface effect. On the models where the C atom is in odd layers (**Figures 12(a,c,e,g,i)**), the magnetic moments of the Mn$_x$ atoms right on top and bottom of the C atom get reduced to less than 2 μ_B, whilst the magnitude of the magnetic moments of the Mn$_y$ atoms in the same atomic plane as the C atom also gets reduced, but by less than 0.1 μ_B. The second-neighbor Mn$_x$-atoms experience an increment of their magnetic moment of up to 0.3 μ_B.

We should pay more attention to the models where the C atom is in even layers (**Figures 12(b,d,f,h)**), however, since those were found to be the most stable (see **Section 4.2.1**). In these models, the magnetic moment of the Mn$_y$ atom on either top or bottom of the C atom is significantly reduced by approximately 0.9 μ_B in all cases. Meanwhile, the 4 Mn$_x$ atoms surrounding the C atom experience a slight reduction in their magnetic moment, while the second neighbors are increased by approximately 0.2 μ_B. It is expected that with a more uniform doping along the whole supercell the enhancement observed in the magnetic moments of second neighbors would become global and reach the values reported by Gutiérrez-Pérez et al. (2017); Holguín-Momaca et al. (2019).

4.2.3 Electronic properties analysis

Figure 13 shows the PDOS by layer of the two stable reconstructions. Only layers 1 to 6 are shown, since the remaining present the same bulk-like behavior. It is clear that the 3d orbitals of the two types of Mn atoms are the main contributors to the states and the magnetism of the structure. Some background states are coming from the Mn 4s, 4p; C 4s, 4p; and Ga 4s, 4p states, but their contribution is insignificant compared to the Mn 3d states. Observe that there is no band gap between the occupied and unoccupied states, revealing the metallic nature of the D0$_{22}$-Mn$_3$Ga. The adsorbed C atom hybridizes with the Mn atom in its same atomic plane at around $-6eV$.

In all cases, it is observed that the Mn$_x$ atoms have most of their spin-up states occupied and the spin-down states unoccupied. This asymmetry with the spin-down states is characteristic of a FM coupling. Nevertheless, it is also observed that the Mn$_y$ atoms have most of their spin-up states unoccupied and the spin-down states occupied, opposite to the Mn$_x$ atoms. This gives us another FM coupling among all the Mn$_y$ atoms but in the opposite sense as the Mn$_x$ ones. The result is that the number of Mn$_x$ ions dominates and yields as a final result a net spin-up magnetic moment, *i.e.* a fM coupling.

Finally, there is not much difference between the B models in **Figures 12(a-f)** and the B.Ga.s$_2$ ones in **Figures 12(g-i)** other than the states at the surface are exclusively generated by Ga atoms in the latter. It can be appreciated in **Figures 12(b,h)** the effect of the surface relaxation and the lattice deformation due to the C incorporation to the surface. The deeper the C atom goes into the surface, the less this point defect disturbs the crystal symmetry.

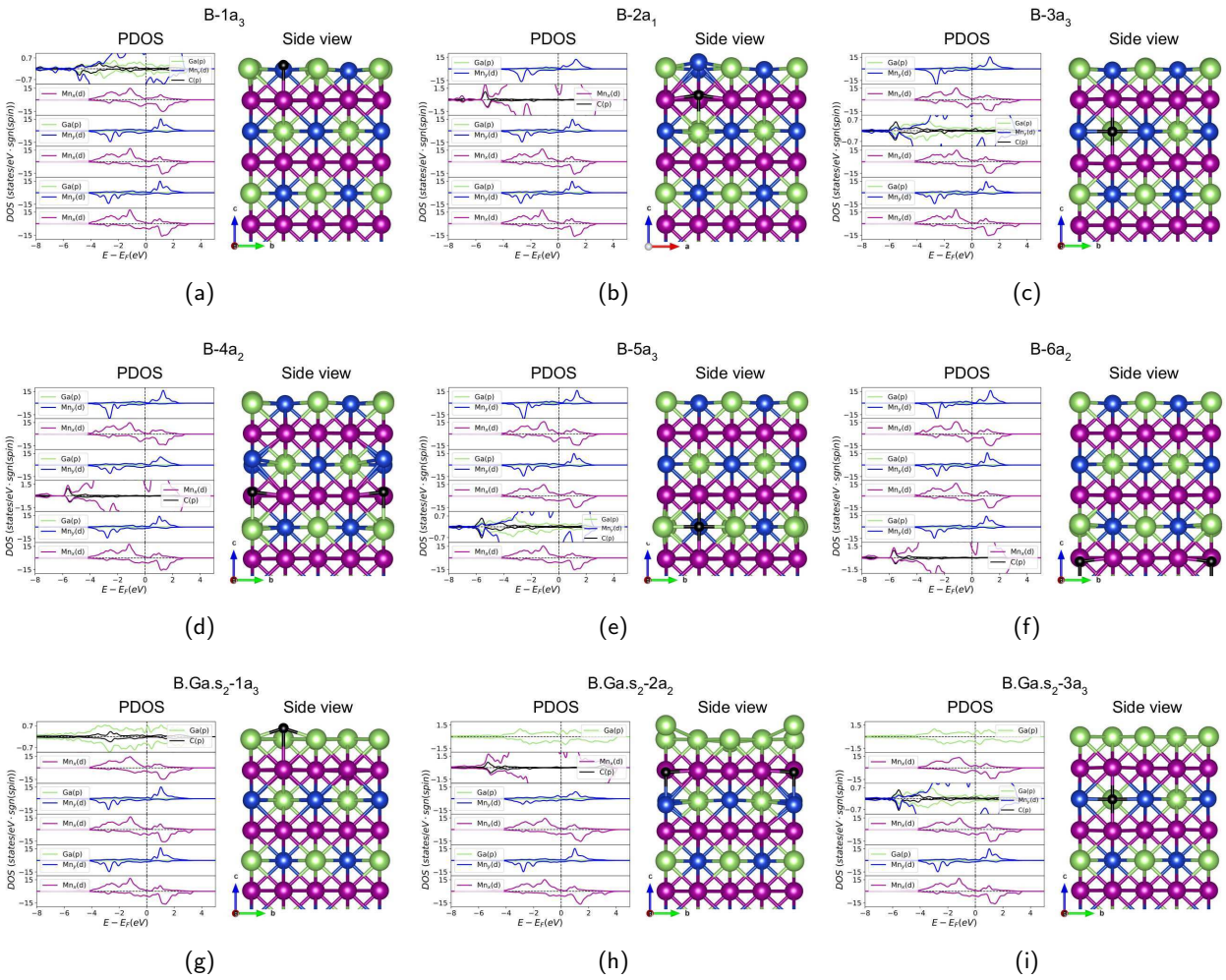

Figure 13. PDOS by layer of the most stable models in D0$_{22}$-Mn$_3$Ga. The information of model B with a C atom in the most stable positions in layers (a) 1, (b) 2, (c) 3, (d) 4, (e) 5, and (f) 6; as well as on model B.Ga.s$_2$ in layers (g) 1, (h) 2, and (i) 3 is shown. Purple, turquoise, dark blue, and black represent the Mn$_x$(d), Ga(p), Mn$_y$(d), and C(p) orbitals contributions' to the DOS, respectively.

4.3 L1$_0$-MnGa

Finally, **Figure 14(a)** shows the final energy vs. unit cell volume of the L1$_0$-MnGa structure. The locations of the Mn and Ga atoms of the L1$_0$-MnGa structure in fractional coordinates are $\left(\frac{1}{2}, \frac{1}{2}, \frac{1}{2}\right)$ and $(0, 0, 0)$, respectively. In this final structure only two possible magnetic orders exist: the FM ground-state and a NM structure. The unit cell volume of the FM structure is 13.40 Å^3/atom, with lattice parameters

$a = b = 2.70$ Å and $c = 3.68$ Å on the DFT model. The ground state energy is $-12.15\ eV/cell$, with a difference of 0.53 $eV/atom$ with the NM configuration. The optimized cell was then taken as a starting point for the DFT+U model with all of the degrees of freedom unconstrained for the calculation and optimization of the stress tensor. The corresponding lattice parameters were $a = b = 2.95$ Å and $c = 4.05$ Å. The calculated magnetic moments of the Mn atoms are: $m_{DFT} = 2.65\mu_B$ and $m_{DFT+U} = 4.41\ \mu_B$. The magnitude of the magnetic moments increases in the DFT+U method because the orbital-dependent term introduced in the +U correction induces strong interactions for the localized Mn(d) states, which are the main responsible for the magnetic properties of the system, as shall be discussed in **Section 4.3.4**.

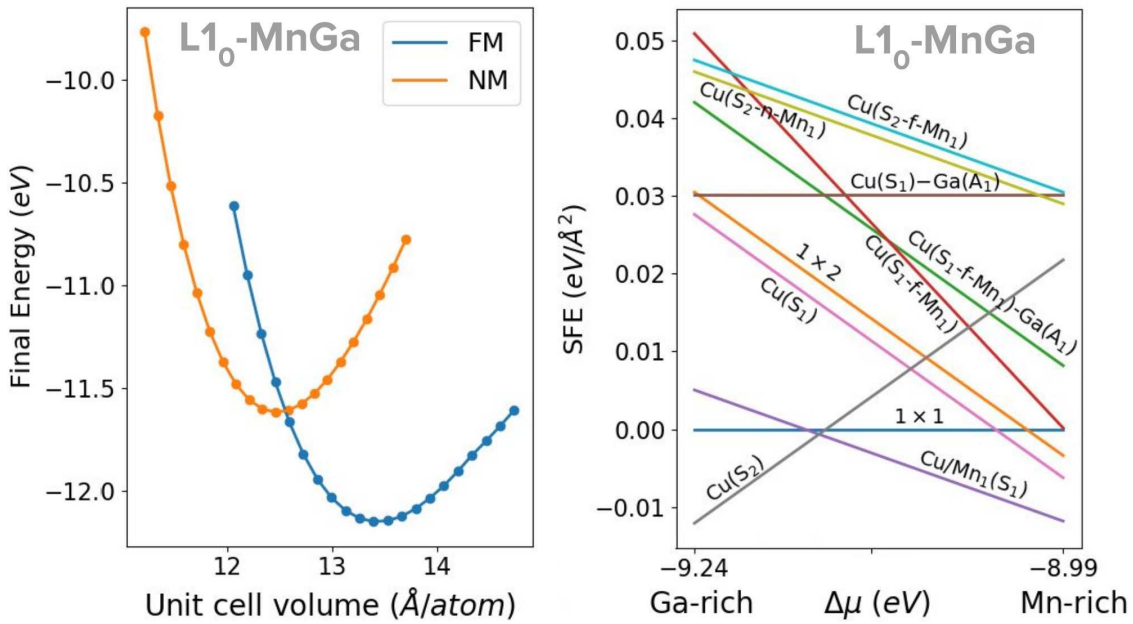

(a) (b)

Figure 14. Stabilities of the L1$_0$-MnGa bulk (in all of its possible magnetic orders) and surface reconstructions: (a) Final energy vs. unit cell volume graph and (b) Surface Formation Energy graph.

The DFT lattice parameter and magnetic moments match almost perfectly other theoretical results, such as the report by Yang et al. (1998). On the experimental side, Xue-Shan et al. (1979) reported lattice parameters $a = b = 2.758$ Å and $c = 3.676$ Å. Corbett et al. (2017) performed a theoretical-experimental study and reported lattice parameters $a = b = 2.83$ Å and $c = 3.68$ Å; and a magnetic moment on the Mn atoms of $m_{DFT} = 2.9\mu_B$. These values have an error smaller than 5 % with both of the calculated models reported in this thesis. The DFT lattice parameters and magnetic moments seem to fit better the data reported in the literature. However, let us keep in mind that the DFT+U models improve the description of the electronic correlation, which will be important for evaluating the electronic properties.

4.3.1 Surface stability analysis

Now is the turn to analyze the adsorption and incorporation of Cu atoms on the most stable $L1_0$-MnGa surfaces. As previously reported by Corbett et al. (2017), $L1_0$-MnGa has two surface terminations: the ideal Ga-terminated 1×1 and the 1×2 row reconstruction with a Mn-by-Ga substitution on the first layer. Considering that both structures are present in the experiment, they were used as the substrates to adsorb and incorporate Cu atoms. The ideal Ga-terminated 1×1 surface was considered first. Model $Cu(A_1)$ is defined containing a Cu atom adsorbed on top of the second-layer Mn atom (position A_1), as labeled in **Figure 6(a)**. Analogously, model $Cu(A_2)$ has a Cu atom adsorbed on top of the first-layer Ga atom (position A_2). Upon comparing the total energy of these sites in **Table 2**, it is evident that $Cu(A_1)$ is more stable than $Cu(A_2)$ by 3.29 eV. Then we consider having atomic exchanges with the first- and second-layer surface atoms. The first case considers Cu atoms incorporated into the first layer. In model $Cu(S_1) - Ga(A_1)$ Ga atoms are kicked out and adsorbed on (A_1) site. Here $Cu(S_1)$ defines a Cu atom substituting a Ga atom of the first surface layer. It is important to remember that only A_1 is considered because it is the most stable surface adsorption site. In the second model ($Cu(S_2) - Mn(A_1)$), the Cu atom takes the place of a second-layer Mn atom, and the ejected Mn adsorbs on the A_1 site. $Cu(S_2)$ stands for a Cu atom substituting a second-layer Mn atom. Considering that $Cu(A_1)$, $Cu(A_2)$, $Cu(S_1) - Ga(A_1)$, and $Cu(S_2) - Mn(A_1)$ have the same number of atoms, we can compare their relative stability through total energies, which are summarized in **Table 2**. Also, all of the models are illustrated in **Figure 21** of the **Annex 2**.

The $Cu(S_1) - Ga(A_1)$ model is more stable than $Cu(S_2) - Mn(A_1)$, $Cu(A_2)$, and $Cu(A_1)$ by 0.90 eV, 3.52 eV, and 0.23 eV, respectively. Finally, we consider the possibility of a direct atom-by-atom substitution via the ejected atoms leaving the surface. Such effect has been experimentally and theoretically observed in other magnetic systems (Guerrero-Sánchez et al., 2015, 2016). Therefore, it exists the possibility in which $Cu(S_1) - Ga(A_1)$ becomes $Cu(S_1)$ and $Cu(S_2) - Mn(A_1)$ becomes $Cu(S_2)$. The SFE formalism was applied just as in the previous alloys.

Following a similar reasoning, we analyze the possibility of adsorbing and incorporating Cu atoms into the 1×2 row reconstruction. Since a surface Mn atom reconstructs the surface, there are more adsorption sites. These are: $Cu - A_1$, $Cu - A_2$, $Cu - A_3$, $Cu - A_4$, $Cu - A_5$, and $Cu - A_6$, as showcased in **Figure 21** of the **Annex 2**. By comparing the relative energies of all these models (see **Table 2**), we notice that the most stable model is $Cu - A_1$. Here the Cu atoms adsorb on top of the second-layer Mn

Table 2. Relative energies of the L1$_0$-MnGa models that have the same number of atoms as the pristine 1×1 and 1×2 surfaces.

Model	Relative energy (eV)
1×1	
$Cu(A_1)$	0.23
$Cu(A_2)$	3.52
$Cu(S_1) - Ga(A_1)$	0.00
$Cu(S_2) - Mn(A_1)$	0.90
1×2	
$Cu - A_1$	0.36
$Cu - A_2$	1.24
$Cu - A_3$	1.30
$Cu - A_4$	0.40
$Cu - A_5$	0.37
$Cu - A_6$	1.19
$Cu(S_1 - f - Mn_1) - Ga(A_1)$	0.00
$Cu(S_1 - f - Mn_1) - Ga(A_2)$	0.76
$Cu(S_1 - f - Mn_1) - Ga(A_3)$	0.53
$Cu(S_1 - f - Mn_1) - Ga(A_4)$	0.25
$Cu(S_1 - f - Mn_1) - Ga(A_5)$	0.18
$Cu(S_1 - f - Mn_1) - Ga(A_6)$	0.60
$Cu(S_1 - n - Mn_1) - Ga(A_1)$	0.18
$Cu(S_2 - n - Mn_1) - Mn(A_1)$	1.37
$Cu(S_2 - f - Mn_1) - Mn(A_1)$	1.32
$Cu/Mn_1(S_1) - Mn_1(A_1)$	2.65
$Cu/Mn_1(S_1) - Mn_1(A_2)$	3.97
$Cu/Mn_1(S_1) - Mn_1(A_3)$	1.83
$Cu/Mn_1(S_1) - Mn_1(A_4)$	0.95
$Cu/Mn_1(S_1) - Mn_1(A_5)$	0.83
$Cu/Mn_1(S_1) - Mn_1(A_6)$	3.89

atoms and near the first-layer Mn atom. Models that arise from considering Cu atomic incorporation as combinations of atomic exchanges were also defined. For example: in model $Cu(S_1 - f - Mn_1) - Ga(A_1)$ the Cu atom takes the place of a Ga atom far from the Mn in the first layer, and the ejected Ga atom adsorbs on position A_1. Letters "f" and "n" stand for "far from" or "near from" the first-layer Mn atom, respectively. The other models are: $Cu(S_1 - n - Mn_1) - Ga(A_1)$, $Cu(S_1 - f - Mn_1) - Ga(A_2)$, $Cu(S_1 - f - Mn_1) - Ga(A_3)$, $Cu(S_1 - f - Mn_1) - Ga(A_4)$, $Cu(S_1 - f - Mn_1) - Ga(A_5)$, $Cu(S_1 - f - Mn_1) - Ga(A_6)$. The relative energies of these systems are presented in **Table 2**. Based on these results, the most stable atomic exchange at the first surface layer is $Cu(S_1 - f - Mn_1) - Ga(A_1)$.

Considering that the atomic exchange of Mn by Cu is not stable in the 1×1 surface (see **Table 2**), some sites in the 1×2 reconstruction were considered. These are: $Cu(S_2 - f - Mn_1) - Mn(A_1)$ and $Cu(S_2 - n - Mn_1) - Mn(A_1)$. The former represents an atomic substitution of a second-layer Mn

far from the first-layer Mn by Cu, and the ejected Mn atom adsorbed on position A_1. The latter is similar, but the exchanged Mn atom is originally located near the first-layer Mn atom. The total energy of these systems is 1.32 eV and 1.37 eV larger than the one most stable energy for S_1 atomic exchange, respectively. This hints that atomic exchanges are less likely and are therefore not considered for the stability analysis.

One more possibility that was considered is that the Cu atom takes the place of the first-layer Mn. The atomic models are: $Cu/Mn_1(S_1) - Mn_1(A_1)$, $Cu/Mn_1(S_1) - Mn_1(A_2)$, $Cu/Mn_1(S_1) - Mn_1(A_3)$, $Cu/Mn_1(S_1) - Mn_1(A_4)$, $Cu/Mn_1(S_1) - Mn_1(A_5)$, and $Cu/Mn_1(S_1) - Mn_1(A_6)$. In the $Cu/Mn_1(S1) - Mn_1(A_1)$ model, the first-layer Mn atom is replaced by a Cu atom, and then it adsorbs on position A_1. The remaining models hold similar descriptions. By comparing the energies of these models, it is clear that the first-layer Mn/Cu atomic exchange is not stable if the Mn atom adsorbs on the surface, following the trend mentioned in **Section 4.2.1**. All calculated models are larger in energy (see **Table 2**). All previously discussed adsorption and incorporation models hold the same number of atoms; therefore, they can be compared directly. The most stable of these models is $Cu(S_1 - f - Mn_1) - Ga(A_1)$.

Finally, other structures were considered in which we take the most stable S_1 and S_2 models — $Cu(S_1 - f - Mn_1) - Ga(A_1)$, $Cu/Mn_1(S_1) - Mn_1(A_5)$, and $Cu(S_2 - n - Mn_1) - Mn(A_1)$ — and remove the adsorbed atoms to generate one–by–one atomic substitutions. These models are $Cu/Mn_1(S_1)$, $Cu(S_1 - f - Mn_1)$, $Cu(S_2 - n - Mn_1)$, and $Cu(S_2 - f - Mn_1)$; in which the Cu atom replaces the first-layer Mn atom, a Ga atom far from the first-layer Mn atom, a second-layer Mn atom that is near to the first-layer Mn atom, and a second-layer Mn atom far from the first-layer Mn atom, respectively. These three models have a different number of atoms compared to the previously discussed models, so the stability of these models cannot be described through total energy differences. In this instance, it is necessary to use the SFE formalism. Considering that the MnGa surfaces are already well described experimentally and theoretically by Corbett et al. (2017), the ideal Ga-terminated 1×1 surface was taken as a reference. Upon including the Mn-induced 1×2 reconstruction to the SFE plot in **Figure 14(b)**, it is clear that this structure is more stable than the ideal Ga-terminated 1×1 surface for Mn-rich conditions, as previously observed by Corbett et al. (2017). Once demonstrated that the stability analysis is correct, some Cu-containing models were included (see **Figure 21** of the **Annex 2** for their graphical representation). The SFE analysis showcases two Cu-containing surfaces as stable. For Mn-rich and intermediate growth conditions, a new 1×2 Cu-induced surface reconstruction — $Cu/Mn_1(S_1)$ — appears as stable, whereas for Ga-rich conditions, a 1×1 surface with Cu atoms incorporated in the second surface layer — $Cu(S_2)$ — achieves stability.

Notice that the new Cu-induced 1×1 surface is Ga-terminated. Although this is a new surface, it will not be discussed further since the 1×2 surface has the potential to be catalytically active due to its Cu atom located in the surface-most layer. Upon increasing the Cu coverage, it is also expected that new stable structures will appear, but that study is beyond the scope of this work. The stability of the surfaces in terms of the Cu coverage is a matter of a separate study. For the rest of this chapter, we will study and compare the properties of both Mn- and Cu- 1×2 single atom surface reconstructions (hereby referred to as Mn and Cu models, respectively).

4.3.2 Structural and STM analysis

Figures 15(a-h) illustrate the top and side views of the four presented models. The difference between the lattice parameter c of the DFT+U and the DFT calculations is clear. **Figure 15(m)** illustrates the surface effect on the relaxation of the modeled structures. The generated surface effect also affects the magnetic and electronic properties, as will be discussed in the coming sections. It is clear that the outermost layer's lattice parameter is different from that of the bulk layers on all models. On the Mn (DFT+U) model, layer 1 expands by 0.5 Å in the $[001]$ direction. Layer 1 contracts by 0.1 Å on the other models. Interestingly, the Mn atom substituted in layer 1 protrudes slightly from the surface, while the Cu atom slightly sinks into it in the DFT+U models. The surface relaxation effect is less noticeable for the DFT models.

Now, **Figures 15(i-l)** show the simulated TH-STM images with a tip distance of 3 Å for occupied states of the four models. The same tip distance and bias were used in the previous study conducted by Corbett et al. (2017). In the Mn-substituted models, the DFT+U surface shows a wavy row-like reconstruction with a high concentration of occupied states around the Ga atoms forming the row. This model has good agreement with the previous report by Corbett et al. (2017). On the other hand, the DFT model of the Mn-substitution does not maintain stable row-like atomic features but forms an array of a square and a rectangular lattice, which was not previously observed experimentally. This showcases the importance of the +U correction for the correct description of these properties of the system. Both Cu-substituted models exhibit that most occupied states are located around the Ga atoms in a roughly row-like periodicity. The DFT+U model shows repeated rows of a centered square array of Ga atoms of nearly equal contrast. Conversely, the center Ga of the central square array exhibits significantly higher contrast in the DFT model.

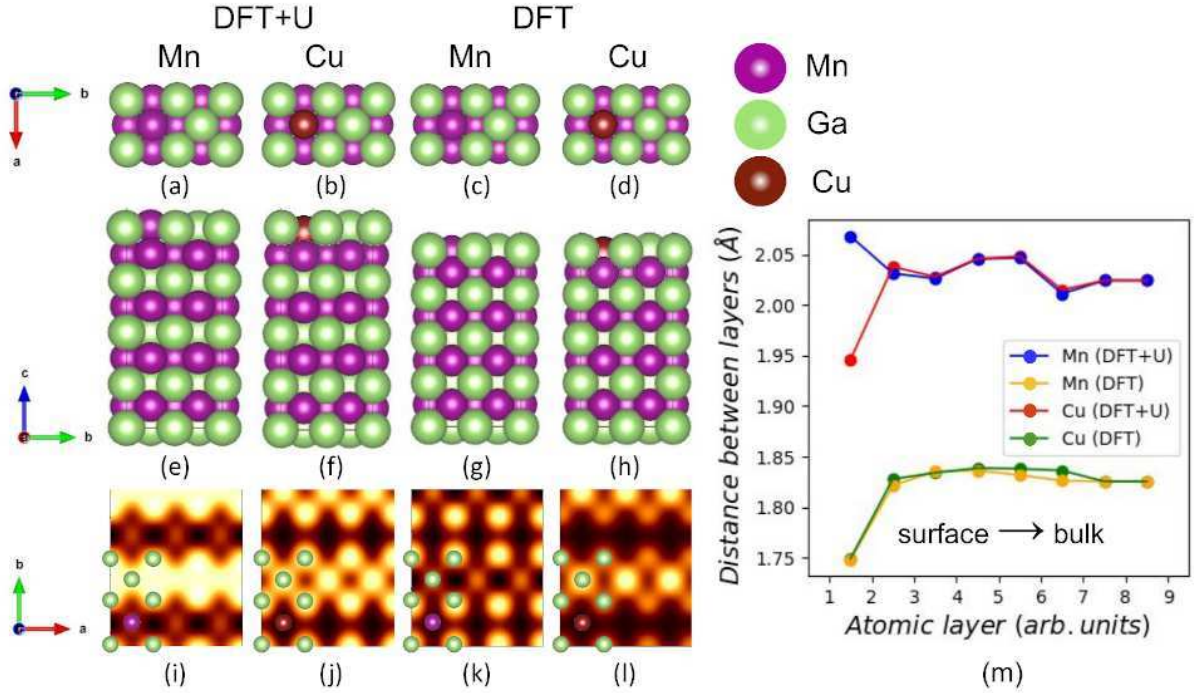

Figure 15. Results from the L1$_0$-MnGa structural relaxation calculations. Top, side and STM ($V = -0.71V$, $d = 3$ Å) views of the (a,e,i) Mn-substituted DFT+U model, (b,f,j) Cu-substituted DFT+U model, (c,g,k) Mn-substituted DFT model, and (d,h,l) Cu-substituted DFT model, respectively. (m) shows quantitative data on the surface relaxation of the models.

4.3.3 Magnetic properties analysis

The L1$_0$-MnGa(001) structure presents a FM behavior with its main contributions coming from Mn atoms. Ga and Cu atoms on the surfaces make an almost-zero contribution in the opposite direction. **Figure 16** shows the magnetic moment analysis per surface layer, from the surface to the bulk, for the four studied surfaces. The values of the bulk magnetic moments are also included for comparison, as horizontal purple (Mn) and turquoise (Ga) lines, respectively.

The surface effect previously mentioned decreases the magnetic moment of the Mn atoms. In **Figures 16(a,b)** the difference is less than 0.1 $\mu_B/atom$, while it is more appreciable in **Figures 16(c,d)** (DFT models) with a difference of up to 0.4 $\mu_B/atom$ in comparison to the bulk. This surface phenomenon is negligible after the second layer. The magnetic moments of the Ga atoms in layer 1 also experience a reduced moment down to nearly zero. The Mn atom substituted onto the Ga layer at the surface couples antiferromagnetically with a magnetic moment of almost the same magnitude as the bulk, as it has been reported Corbett et al. (2017). Interestingly, the magnetic moment of the Cu atom substituted onto the surface shifts to a positive value, but its magnitude remains close to zero.

It is worth recalling that the DFT+U method improves the description of strongly localized electrons by introducing an orbital-dependent term known as the on-site Coulomb repulsion energy (U) into the exchange-correlation term. The interactions derived from this term are particularly strong for localized d and f electrons, such as those in Mn(d) and Cu(d) states, the former of which are the main ones responsible for the magnetic properties of the system. This causes the difference in the magnitudes of the Mn magnetic moments between the DFT and DFT+U models. This is a well-known phenomenon that has been reported, for instance, in Fe and Ni monoxides, Fayalite, and (in a more related fashion to the materials in the present study) metallic Fe, Ni, and Ce (Cococcioni and de Gironcoli, 2005; Himmetoglu et al., 2014). However, by improving the description of strongly localized electrons, the DFT+U method allows us to describe their properties more closely to reality. Particularly in this thesis, the +U correction was used to compare its effect on the potential catalytic behavior of Cu. It is found that both DFT and DFT+U frameworks show the same behavior and lead to the same conclusions.

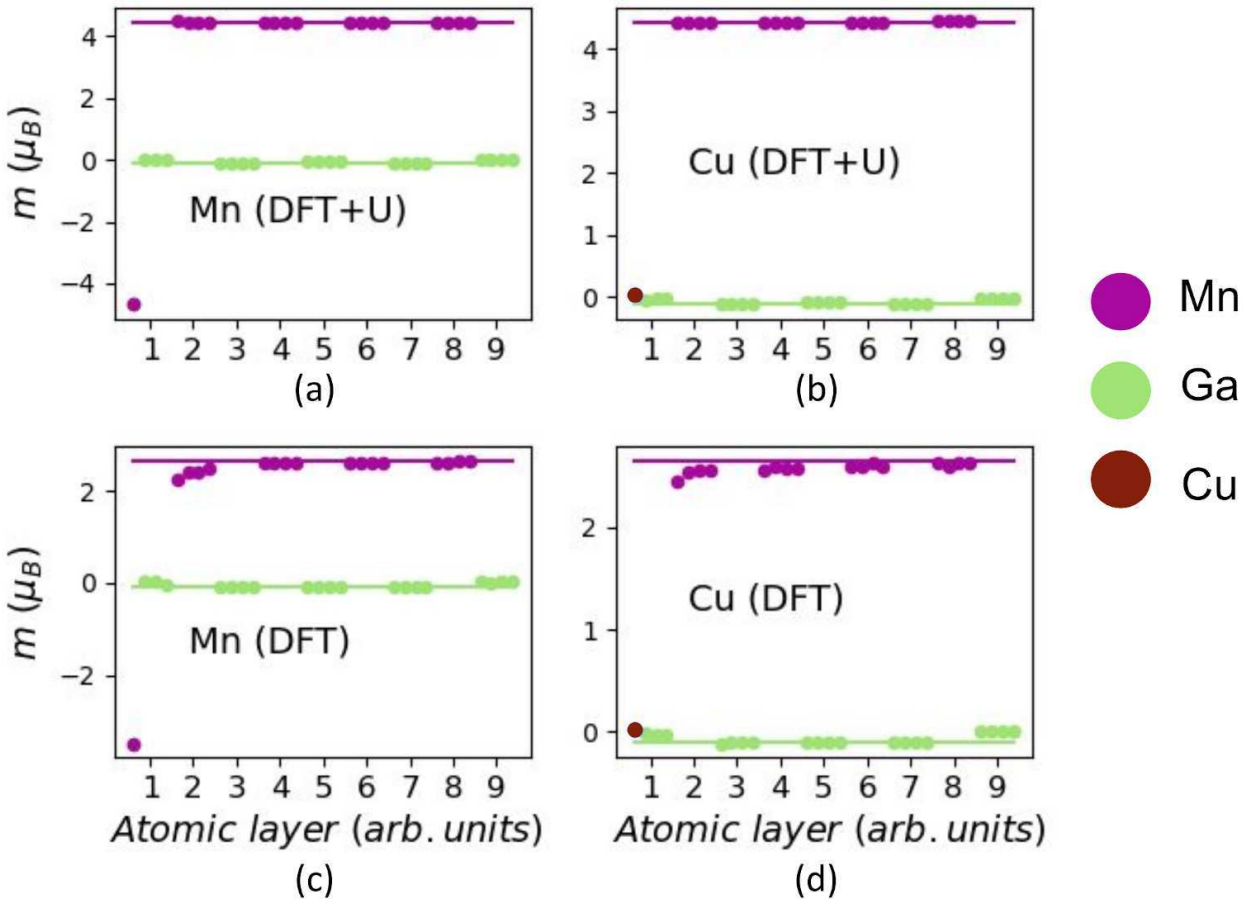

Figure 16. Analysis of the surface magnetic moments per layer of the (a) Mn-substituted DFT+U model, (b) Cu-substituted DFT+U model, (c) Mn-substituted DFT model, and (d) Cu-substituted DFT model. Horizontal solid lines show the values of the magnetic moments from the bulk calculations of the Mn and Ga atoms, respectively.

4.3.4 Electronic properties analysis

Figure 17 shows the PDOS of each atomic layer of the four calculated structures. Only layers 1 to 4 are shown, as the remaining present the same bulk-like behavior. In all models, the width of the spin-up band is narrower than the spin-down band, as reported by Yang et al. (1998), which is associated with a less strong bonding of the spin-down electrons and thus a stronger interaction among themselves. Analysis of the PDOS reveals that the Mn 3d states govern the electronic states and the magnetic structure at the Mn-layers. These states generate the characteristic peak structures of $L1_0$-MnGa (Jain et al., 2020; Garcia-Diaz et al., 2017). Some background states are coming from the Mn 4s and Ga 4s, 4p states, but their contribution is not significant compared to the Mn 3d states. The Ga-layers do not contribute significantly to the DOS of any structure.

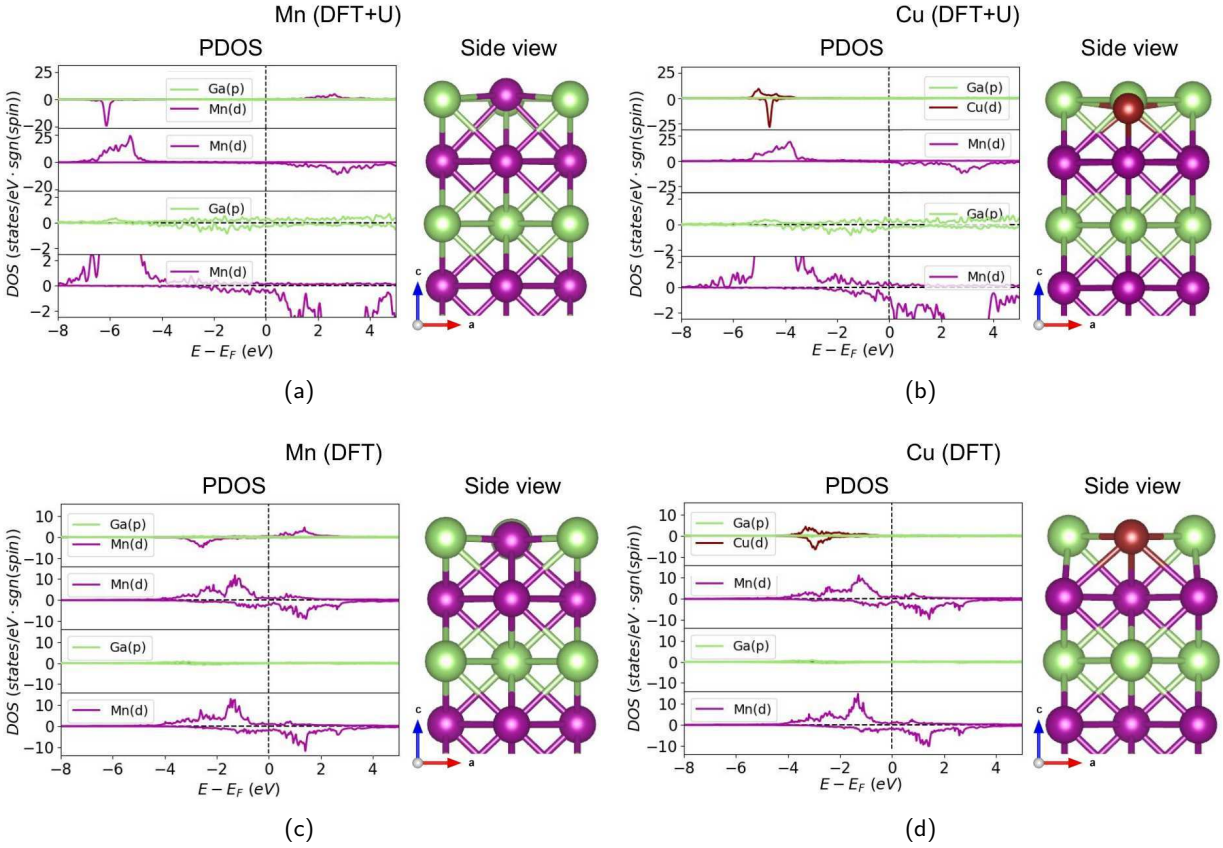

Figure 17. PDOS by layer of the most stable models in $L1_0$-MnGa: (a) Mn (DFT+U), (b) Cu (DFT+U), (c) Mn (DFT), and (d) Cu (DFT). Purple, turquoise, and brown represent the Mn(d) orbitals, Ga(p) orbitals, and Cu(d) orbitals contributions' to the DOS, respectively.

Compared to the DFT models, the DFT+U models show a shift of the occupied and unoccupied states away from the Fermi level. This occurs because the incorporation of the Hubbard correction results in an overestimation of the binding energy in the d-state, which results in under-hybridization with the

valence states (Harun et al., 2020). This effect has been previously reported (Ryee and Han, 2018; Musa Saad H.-E. and Anwar K Abdelhalim, 2020). However, it is worth noting that all MnGa models possess metallic behavior. In the DFT+U models, the y-axis was zoomed on layers far from the surface in order to appreciate the DOS near the Fermi level. The metallic behavior of all models is confirmed by analyzing the ELF's 2D cuts displayed in **Figure 18** for both spin-up and spin-down states of the front and middle sections of the slabs.

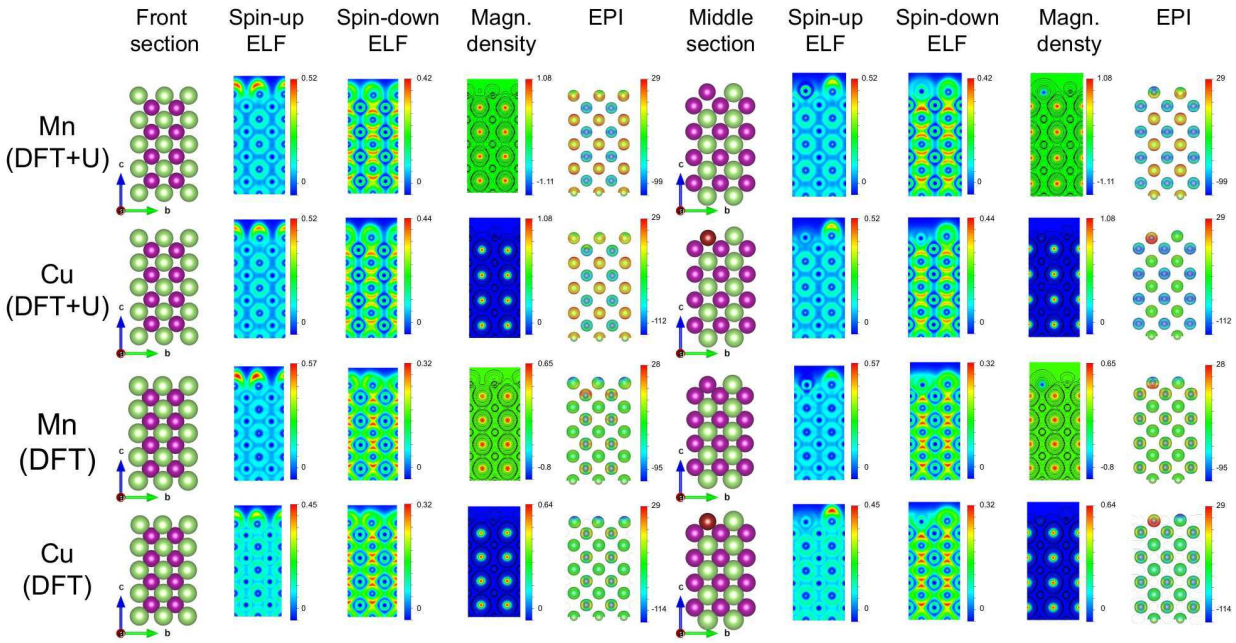

Figure 18. Atomic model, ELFs, magnetization density and EPI (isosurface value $= 0.05\ e/a.u.^3$) of the front and middle sections of all the simulated slabs.

The metallic behavior is reflected when noticing that on all subfigures, there is a region where the ELFs have a constant-like behavior, as stated by Koumpouras and Larsson (2020). Also, by considering the bonding localization window for each image, it is clear that all of them have a value < 0.7, falling into the metallic category. Interestingly, the symmetry breaking from the surface leads to high localization of spin-up electrons on top of the Ga atoms at the surface, which is consistent with the previously analyzed STM images.

The magnetization density (defined in **Section 2.9**) is shown in **Figure 18**. It reaches a minimal value at the empty space between atoms and the location of the Ga and Cu atoms, demonstrating their diamagnetic nature. It also displays a positive value for all Mn atoms except for the one substituted at the surface, which has a negative one. This is a visual representation of the already previously examined antiferromagnetic coupling of this atom with the rest of the structure. Finally, **Figure 18** shows the EPI

at a value $0.05\ e/a.u.^3$. It is clear that the substituted Cu atoms have a highly positive charge distribution on both models *i.e.* they are electronegative. This particular surface structure could potentially interact with electropositive sites of molecules at Cu ends — since Cu will have a tendency to attract electrons — and electronegative sites of molecules at Ga ends — since these sites of the molecules will attract the localized electrons at the surface above Ga. This creates ideal conditions for catalytic reactions to be carried out at the surface, making this structure a Single-Atom Alloy Catalyst.

There are some instances of the use of metallic Ga as catalysts. For example, Qin and Schneider (2016) reported the use of elemental Ga as a catalyst for the formation of saturated bonds with high chemoselectivity. Toyir et al. (2001a,b,c) conducted a series of studies on a highly effective conversion of CO_2 to methanol over Ga-promoted Cu-based catalysts. Furthermore, with the $L1_0$-MnGa being a ferromagnet, its intrinsic magnetic field could further boost its catalytic properties by interacting with the spin state of the reactants and favorably influencing the energy levels of their atomic species.

Chapter 5. Conclusions

Throughout this thesis, the results of a series of first-principles DFT calculations were presented, seeking to characterize the structural, electronic, and magnetic properties of the bulk and the (001) surfaces of three Mn-Ga alloys. In the α-Mn, atomic coordinates and magnetic moments of a CL-AFM order at the ground and a NCL-AFM state under stretching strain were characterized. A surface analysis was performed to match all the possible theoretical (001) surface reconstructions to experimental STM images. It was determined that only layers 6, 8 and 10 can reproduce the experimentally-observed square- and row- reconstructions. The two models based on layer 6 explained the experimental data most correctly, as they have the lowest surface formation energies of the aforementioned models and are the only ones with the same Fast Fourier Transform patterns as the experimental images. An analysis of the magnetic moments of these two models revealed spin canting at the square-reconstruction and a total projection of the spins onto the surface plane for the row-reconstruction, which are entirely due to the surface effect and strongly resembled previous experimental studies. Further theoretical studies are required to characterize the third large-row-vacancy-reconstruction observed experimentally and possibly simulate the proposed surfaces with a NCL-AFM bulk configuration.

Also, a comprehensive analysis of the $D0_{22}$-Mn_3Ga structure was performed. It was determined that the structure behaves as a fM and its magnetic behavior was dependent on the Mn atoms. Each atom's positions and magnetic moments were determined and found in good agreement with previous studies. All the possible first-layer (001) surface reconstructions were examined, and it was determined that two 1×1 reconstructions (one Mn_y-Ga-terminated and the other Ga-terminated) were the most stable. The surface effect strongly affected the magnetic moments of the surface-most two layers, and a very localized effect of the C doping on the magnetic moments was observed decreasing the magnetic moments of the first-neighbor Mn atoms and increasing the magnetic moments of the second-neighbor Mn atoms. The experimental enhancement of the magnetization of the structure due to C doping was explained in terms of a superexchange interaction among the two Mn_x atoms and a C atom incorporated in the most stable octahedral positions. The PDOS revealed the nature of the fM behavior and its enhancement.

Finally, the most stable $L1_0$-MnGa(001) surface reconstructions with Mn and Cu were presented. A study on the bulk structures determined that this alloy is FM and also its lattice parameters. The most stable structures were 1×1 and 1×2 Cu-substituted models, but only the 1×2 reconstruction was studied because of the potential catalytic applications due to its Cu atom located in the surface-most layer. The properties of another previously reported 1×2 reconstruction were compared. It was found

that both surfaces display a row-like pattern when observed via STM images. It was also shown that the surfaces behave very similarly to the bulk, except for when a Mn atom is substituted at the surface, in which case it is coupled in an AFM fashion. The newfound 1×2 Cu-substituted structure is a good candidate for heterogeneous catalysis thanks to its surface behavior: it has a high localization of spin-up electrons above the Ga atoms and the Cu atom behaves electronegatively. The surfaces were studied with both DFT+U and DFT theories and the results lead to the same conclusion regarding the potential for catalysis. Further studies are required to test the catalytic potential of this surface and characterize the properties of the 1×1 and other surfaces richer in Cu.

Bibliography

Al-Aqtash, N. and Sabirianov, R. (2015). Strain control of magnetocrystalline anisotropy and energy product of mnga alloys. *Journal of Magnetism and Magnetic Materials*, 391:26–33.

Ando, K., Fujita, S., Ito, J., Yuasa, S., Suzuki, Y., Nakatani, Y., Miyazaki, T., and Yoda, H. (2014). Spin-transfer torque magnetoresistive random-access memory technologies for normally off computing (invited). *Journal of Applied Physics*, 115(17):172607.

Anisimov, V. I., Zaanen, J., and Andersen, O. K. (1991). Band theory and mott insulators: Hubbard u instead of stoner i. *Phys. Rev. B*, 44:943–954.

Balke, B., Fecher, G. H., Winterlik, J., and Felser, C. (2007). Mn3ga, a compensated ferrimagnet with high curie temperature and low magnetic moment for spin torque transfer applications. *Applied Physics Letters*, 90(15):152504.

Becke, A. D. and Edgecombe, K. E. (1990). A simple measure of electron localization in atomic and molecular systems. *The Journal of Chemical Physics*, 92(9):5397–5403.

Blöchl, P. E. (1994). Projector augmented-wave method. *Phys. Rev. B*, 50:17953–17979.

Blöchl, P. E., Jepsen, O., and Andersen, O. K. (1994). Improved tetrahedron method for brillouin-zone integrations. *Phys. Rev. B*, 49:16223–16233.

Bottyan, T. (2020). Electrostatic potential maps. `https://chem.libretexts.org/Bookshelves/Physical_and_Theoretical_Chemistry_Textbook_Maps/Supplemental_Modules_(Physical_and_Theoretical_Chemistry)/Chemical_Bonding/Fundamentals_of_Chemical_Bonding/Electrostatic_Potential_maps`.

Bradley, A. J. and Thewlis, J. (1927). *Proceedings of the Royal Society of London. Series A, Containing Papers of a Mathematical and Physical Character*, 115(771):456–471.

Brown, D. R., Han, K., Siegrist, T., Besara, T., and Niu, R. (2016a). High magnetic field annealing of mn-ga intermetallic alloys. *MRS Advances*, 1(3):227–233.

Brown, D. R., Han, K., Siegrist, T., Besara, T., and Niu, R. (2016b). Magnetic properties of doped mn-ga alloys made by mechanical milling and heat treatment. *AIP Advances*, 6(5):056012.

Busch, T., Englert, B.-G., Rzażewski, K., and Wilkens, M. (1998). Two cold atoms in a harmonic trap. *Foundations of Physics*, 28(4):549–559.

Capelle, K. (2006). A bird's-eye view of density-functional theory. *Brazilian Journal of Physics*, 36(4a):1318–1343.

Cococcioni, M. and de Gironcoli, S. (2005). Linear response approach to the calculation of the effective interaction parameters in the $\mathrm{LDA+U}$ method. *Phys. Rev. B*, 71:035105.

Corbett, J., Guerrero-Sanchez, J., Richard, A., Ingram, D., Takeuchi, N., and Smith, A. (2017). Surface structures of l_{10}-mnga (001) by scanning tunneling microscopy and first-principles theory. *Applied Surface Science*, 422:985–989.

Côté, M. (2008). Introduction to dft+u. `https://pitp.phas.ubc.ca/confs/sherbrooke/archives/pitpcifar_sherbrooke2008_dft_u_cote.pdf`.

de la Roza, A. O., Johnson, E. R., and Luaña, V. (2014). Critic2: A program for real-space analysis of quantum chemical interactions in solids. *Computer Physics Communications*, 185(3):1007–1018.

Dudarev, S. L., Botton, G. A., Savrasov, S. Y., Humphreys, C. J., and Sutton, A. P. (1998). Electron-energy-loss spectra and the structural stability of nickel oxide: An lsda+u study. *Phys. Rev. B*, 57:1505–1509.

Elliott, R., Coley, K., Mostaghel, S., and Barati, M. (2018). Review of manganese processing for production of trip/twip steels, part 1: Current practice and processing fundamentals. *JOM*, 70(5):680–690.

Emsley, J. (2011). *Nature's building blocks: an A-Z guide to the elements*. Oxford University Press, new ed., completely rev. and updated edition.

Encyclopedia Britannica (2010). Manganese. `https://www.britannica.com/science/manganese`.

Flores, M. A., Orellana, W., and Menéndez-Proupin, E. (2018). Accuracy of the heyd-scuseria-ernzerhof hybrid functional to describe many-electron interactions and charge localization in semiconductors. *Phys. Rev. B*, 98:155131.

Frijns, A. J., Rindt, C. C., and Gaastra-Nedea, S. V. (2021). 17 - modeling thermochemical reactions in thermal energy storage systems. In Cabeza, L. F., editor, *Advances in Thermal Energy Storage Systems (Second Edition)*, Woodhead Publishing Series in Energy, pages 497–542. Woodhead Publishing, second edition edition.

Garcia-Diaz, R., Cocoletzi, G. H., Mandru, A.-O., Wang, K., Smith, A. R., and Takeuchi, N. (2017). Structural, electronic and magnetic properties of the mnga(111)-1×2 and 2×2 reconstructions: Spin polarized first principles total energy calculations. *Applied Surface Science*, 419:286–293.

Goldschmidt, H. (1967). *Interstitial Alloys*. Butterworth-Heinemann.

Goodenough, J. B. (2008). Goodenough-Kanamori rule. *Scholarpedia*, 3(10):7382. revision #122456.

Griffiths, D. J. (1995). *Introduction to quantum mechanics*. Prentice Hall, Englewood Cliffs, N.J.

Grunebohm, A., Herper, H. C., Gruner, M. E., and Entel, P. (2009). Suitability of fe/gaas and (co,ni)mn(ga,ge) for spintronics applications: An ¡emphasis emphasistype="boldital"¿ab initio¡/emphasis¿ study. *IEEE Transactions on Magnetics*, 45(10):3965–3968.

Guerrero-Sánchez, J., Mandru, A.-O., Takeuchi, N., H. Cocoletzi, G., and Smith, A. R. (2016). Understanding the stability of fe incorporation within mn3n2(001) surfaces: An ab-initio study. *Applied Surface Science*, 363:651–658.

Guerrero-Sánchez, J., Mandru, A.-O., Wang, K., Takeuchi, N., Cocoletzi, G. H., and Smith, A. R. (2015). Structural, electronic and magnetic properties of mn3n2(0 0 1) surfaces. *Applied Surface Science*, 355:623–630.

Gutiérrez-Pérez, R., Holguín-Momaca, J., Santillán-Rodríguez, C., López Antón, R., Ochoa-Lara, M., Flores-Holguín, N., Espinosa-Magaña, F., Matutes-Aquino, J., and Olive-Méndez, S. (2017). High enhanced magnetization in carbon-doped mn3ga thin films. *Intermetallics*, 88:14–18.

H. W. H. (1927). The resources and applications of manganese. *Nature*, 120(3013):159–161.

Hao, L. and Xiong, W. (2020). An evaluation of the mn–ga system: Phase diagram, crystal structure, magnetism, and thermodynamic properties. *Calphad*, 68:101722.

Hargittai, B. and Hargittai, I. (2019). Year of the periodic table: Mendeleev and the others. *Structural Chemistry*, 30(1):1–7.

Harun, K., Salleh, N. A., Deghfel, B., Yaakob, M. K., and Mohamad, A. A. (2020). Dft+u calculations for electronic, structural, and optical properties of zno wurtzite structure: A review. *Results in Physics*, 16:102829.

Herrmann, C., Solomon, G. C., and Ratner, M. A. (2010). Organic radicals as spin filters. *Journal of the American Chemical Society*, 132(11):3682–3684.

Himmetoglu, B., Floris, A., de Gironcoli, S., and Cococcioni, M. (2014). Hubbard-corrected dft energy functionals: The lda+u description of correlated systems. *International Journal of Quantum Chemistry*, 114(1):14–49.

Hobbs, D., Hafner, J., and Spisak, D. (2003). Understanding the complex metallic element mn. i. crystalline and noncollinear magnetic structure of α-mn. *Physical Review B*, 68(1):014407.

Hodgson, M. J. P. (2021). Analytic solution to the time-dependent schrödinger equation for the one-dimensional quantum harmonic oscillator with an applied uniform field.

Hohenberg, P. and Kohn, W. (1964). Inhomogeneous electron gas. *Phys. Rev.*, 136:B864–B871.

Holguín-Momaca, J. T., Gutiérrez Pérez, R. M., Reyes-Rojas, A., Espinosa-Magaña, F., López Antón, R., and Olive-Méndez, S. F. (2019). Study of carbon-doped mn3ga thin films with enhanced magnetization. *Intermetallics*, 104:90–96.

Hubbard, J. (1963). Electron correlations in narrow energy bands. *Proceedings of the Royal Society of London. Series A. Mathematical and Physical Sciences*, 276:238—-257.

Hunter, J. D. (2007). Matplotlib: A 2d graphics environment. *Computing in Science & Engineering*, 9(3):90–95.

Ishkhanyan, A. M. (2015). Exact solution of the schrödinger equation for the inverse square root potential $v_0/\sqrt{x}$. *EPL (Europhysics Letters)*, 112(1):10006.

Jacob, C. R. and Reiher, M. (2012). Spin in density-functional theory. *International Journal of Quantum Chemistry*, 112(23):3661–3684.

Jain, A., Ong, S. P., Hautier, G., Chen, W., Richards, W. D., Dacek, S., Cholia, S., Gunter, D., Skinner, D., Ceder, G., and et al. (2013). Commentary: The materials project: A materials genome approach to accelerating materials innovation. *APL Materials*, 1(1):011002.

Jain, A., Ong, S. P., Hautier, G., Chen, W., Richards, W. D., Dacek, S., Cholia, S., Gunter, D., Skinner, D., Ceder, G., and Persson, K. a. (2020). Materials data on mnga by materials project.

Jeschke, G. and Polyhach, Y. (2007). Distance measurements on spin-labelled biomacromolecules by pulsed electron paramagnetic resonance. *Physical Chemistry Chemical Physics*, 9(16):1895.

Kanamori, J. (1959). Superexchange interaction and symmetry properties of electron orbitals. *Journal of Physics and Chemistry of Solids*, 10(2):87–98.

Kasper, J. S. and Roberts, B. W. (1956). Antiferromagnetic structure of -manganese and a magnetic structure study of -manganese. *Physical Review*, 101(2):537–544.

Katine, J. and Fullerton, E. E. (2008). Device implications of spin-transfer torques. *Journal of Magnetism and Magnetic Materials*, 320(7):1217–1226.

Kato, T. (1957). On the eigenfunctions of many-particle systems in quantum mechanics. *Communications on Pure and Applied Mathematics*, 10(2):151–177.

Kaufman, J. G. (2000). *Introduction to aluminum alloys and tempers*. ASM International.

Koch, W. and Holthausen, M. C. (2001). *A Chemist's Guide to Density Functional Theory*. Wiley, 1 edition.

Kohn, W. and Sham, L. J. (1965). Self-consistent equations including exchange and correlation effects. *Phys. Rev.*, 140:A1133–A1138.

Koumpouras, K. and Larsson, J. A. (2020). Distinguishing between chemical bonding and physical binding using electron localization function (ELF). 32(31):315502.

Kresse, G. and Furthmüller, J. (1996). Efficient iterative schemes for ab initio total-energy calculations using a plane-wave basis set. *Phys. Rev. B*, 54:11169–11186.

Kresse, G. and Furthmüller, J. (2022a). The vasp manual - calculation setup - incar tags - ediff. `https://www.vasp.at/wiki/index.php/EDIFF`.

Kresse, G. and Furthmüller, J. (2022b). The vasp manual - calculation setup - incar tags - ediffg. `https://www.vasp.at/wiki/index.php/EDIFFG`.

Kresse, G. and Furthmüller, J. (2022c). The vasp manual - calculation setup - incar tags - locpot. `https://www.vasp.at/wiki/index.php/LOCPOT`.

Kresse, G. and Joubert, D. (1999). From ultrasoft pseudopotentials to the projector augmented-wave method. *Phys. Rev. B*, 59:1758–1775.

Krén, E. and Kádár, G. (1970). Neutron diffraction study of mn3ga. *Solid State Communications*, 8(20):1653–1655.

Kunitomi, N., Yamada, T., Nakai, Y., and Fujii, Y. (1969). Preparation of [U+2010]manganese single crystals and their physical properties. *Journal of Applied Physics*, 40(3):1265–1269.

Lawson, A. C., Larson, A. C., Aronson, M. C., Johnson, S., Fisk, Z., Canfield, P. C., Thompson, J. D., and Von Dreele, R. B. (1994). Magnetic and crystallographic order in [U+2010]manganese. *Journal of Applied Physics*, 76(10):7049–7051.

Lewis, L. H. and Jiménez-Villacorta, F. (2013). Perspectives on permanent magnetic materials for energy conversion and power generation. *Metallurgical and Materials Transactions A*, 44(1):2–20.

Lu, L., Hu, H., Hou, H., and Wang, B. (2013). An improved b3lyp method in the calculation of organic thermochemistry and reactivity. *Computational and Theoretical Chemistry*, 1015:64–71.

Lu, X., Liang, J., Shi, T., and Zhou, M. (1980). A x-ray investigation of the manganese-gallium system. *Acta Phys. Sin.*, 29:469–484.

Ma, Q., Sugihara, A., Suzuki, K., Zhang, X., Miyazaki, T., and Mizukami, S. (2014). Tetragonal heusler-like mn – ga alloys based perpendicular magnetic tunnel junctions. *SPIN*, 04(04):1440024.

Ma, Q. L., Kubota, T., Mizukami, S., Zhang, X. M., Naganuma, H., Oogane, M., Ando, Y., and Miyazaki, T. (2013). Interface tailoring effect on magnetic properties and their utilization in mnga-based perpendicular magnetic tunnel junctions. *Phys. Rev. B*, 87:184426.

Maldonado-Lopez, D., Takeuchi, N., and Guerrero-Sanchez, J. (2021). Understanding the noncollinear antiferromagnetic irmn 3 surfaces and their exchange-biased heterostructures from first-principles. *ACS Applied Electronic Materials*, 3(3):1086–1096.

Mao, S., Lu, J., Zhao, X., Wang, X., Wei, D., Liu, J., Xia, J., and Zhao, J. (2017). Mnga-based fully perpendicular magnetic tunnel junctions with ultrathin co2mnsi interlayers. *Scientific Reports*, 7(1):43064.

March, N. H. (1986). Spatially dependent generalization of kato's theorem for atomic closed shells in a bare coulomb field. *Phys. Rev. A*, 33:88–89.

Masumoto, H., Watanabe, K., and Mitera, M. (1978). Equilibrium diagram of mnndash;ga binary alloys. *Transactions of the Japan Institute of Metals*, 19(7):395–399.

Materials Project (2013a). Materials data on α-mn. `https://materialsproject.org/materials/mp-35/`.

Materials Project (2013b). Materials data on d0_{22}-mn_3ga. `https://materialsproject.org/materials/mp-1210627/#`.

Materials Project (2013c). Materials data on ga. `https://materialsproject.org/materials/mp-142/#`.

Materials Project (2013d). Materials data on l1_0-mnga. `https://materialsproject.org/materials/mp-1001836/#`.

Meissner, H. G., Schubert, K., and Anantharaman, T. R. (1965). The constitution and structure of manganese-gallium alloys. *Proceedings of the Indian Academy of Sciences - Section A*, 61(6):340–367.

Methfessel, M. and Paxton, A. T. (1989). High-precision sampling for brillouin-zone integration in metals. *Phys. Rev. B*, 40:3616–3621.

Minakuchi, K., Umetsu, R. Y., Ishida, K., and Kainuma, R. (2012). Phase equilibria in the mn-rich portion of mn–ga binary system. *Journal of Alloys and Compounds*, 537:332–337.

Mix, T., Müller, K.-H., Schultz, L., and Woodcock, T. (2015). Formation and magnetic properties of the l10 phase in bulk, powder and hot compacted mn–ga alloys. *Journal of Magnetism and Magnetic Materials*, 391:89–95.

Momma, K. and Izumi, F. (2011). *VESTA3* for three-dimensional visualization of crystal, volumetric and morphology data. *Journal of Applied Crystallography*, 44(6):1272–1276.

Monkhorst, H. J. and Pack, J. D. (1976). Special points for brillouin-zone integrations. *Phys. Rev. B*, 13:5188–5192.

Musa Saad H.-E., M. and Anwar K Abdelhalim, M. (2020). Dft and dft+u investigation of the effect of spin–orbit interaction and exchange-correlation energy on electronic and magnetic structures of ir-based double perovskites ba 2 tiro 6 (t = cr, mn, and fe). *AIP Advances*, 10(3):035027.

Nave, C. R. (2000). Pauli exclusion principle. `http://hyperphysics.phy-astr.gsu.edu/hbase/pauli.html`.

Nemec, L. and Hofmann, O. T. (2014). The basics of dft. `http://helper.ipam.ucla.edu/publications/gss2014/gss2014_12166.pdf`.

Niida, H., Hori, T., Onodera, H., Yamaguchi, Y., and Nakagawa, Y. (1996). Magnetization and coercivity of mn3−ga alloys with a d022-type structure. *Journal of Applied Physics*, 79(8):5946.

Oberteuffer, J., Marcus, J., Schwartz, L., and Felcher, G. (1968). Magnetic structure of a single crystal of alpha manganese. *Physics Letters A*, 28(4):267–268.

Pan, F., Pflitsch, C., David, R., Verheij, L., and Franchy, R. (2001). Formation of an ordered oxide on the coga(100) surface by room temperature oxidation and annealing. *Surface Science*, 479(1):191–200.

Perdew, J. P., Burke, K., and Ernzerhof, M. (1996). Generalized gradient approximation made simple. *Phys. Rev. Lett.*, 77:3865–3868.

Preuss, E., Krahl-Urban, B., and Butz, R. (1974). *Crystal Structures of the Elements*. Vieweg+Teubner Verlag.

Prinz, G. A. (1990). Hybrid ferromagnetic-semiconductor structure. *Science*, 250(4984):1092–1097.

Qian, G.-X., Martin, R. M., and Chadi, D. J. (1988). First-principles study of the atomic reconstructions and energies of ga- and as-stabilized gaas(100) surfaces. *Phys. Rev. B*, 38:7649–7663.

Qin, B. and Schneider, U. (2016). Catalytic use of elemental gallium for carbon–carbon bond formation. *Journal of the American Chemical Society*, 138(40):13119–13122.

Royal Society of Chemistry (2021). Manganese. `https://www.rsc.org/periodic-table/element/25/manganese#:~:text=Manganese(IV)%20oxide%20is%20used,to%20make%20fertilisers%20and%20ceramics`.

Ruvalcaba, R., Corbett, J. P., Mandru, A.-O., Takeuchi, N., Smith, A. R., and Guerrero-Sanchez, J. (2021). Surface structures of magnetostrictive d03-fe3ga(001). *Applied Surface Science*, 553:149488.

Ryee, S. and Han, M. J. (2018). The effect of double counting, spin density, and hund interaction in the different dft+u functionals. *Scientific Reports*, 8(1):9559.

Schay, G. (2012). *A Concise Introduction to Linear Algebra*. Birkhäuser Boston, Boston, MA.

Scott, T. and Zhang, W. (2015). Efficient hybrid-symbolic methods for quantum mechanical calculations. *Computer Physics Communications*, 191:221–234.

Sever, R., Bucurgat, M., Tezcan, C., and Yeşiltaş, [U+FFFD] (2008). Bound state solution of the schrödinger equation for mie potential. *Journal of Mathematical Chemistry*, 43(2):749–755.

Shull, C. G. and Wilkinson, M. K. (1953). Neutron diffraction studies of various transition elements. *Reviews of Modern Physics*, 25(1):100–107.

Silvi, B. and Savin, A. (1994). Classification of chemical bonds based on topological analysis of electron localization functions. *Nature*, 371(6499):683–686.

Sinitsyn, N. A. and Chernyak, V. Y. (2017). The quest for solvable multistate landau-zener models. *Journal of Physics A: Mathematical and Theoretical*, 50(25):255203.

Slater, J. C. (1964). Atomic radii in crystals. *The Journal of Chemical Physics*, 41(10):3199–3204.

Sliwko, V., Mohn, P., and Schwarz, K. (1994). The electronic and magnetic structures of alpha - and beta -manganese. *Journal of Physics: Condensed Matter*, 6(32):6557–6564.

Solovyev, I. V., Dederichs, P. H., and Anisimov, V. I. (1994). Corrected atomic limit in the local-density approximation and the electronic structure of d impurities in rb. *Phys. Rev. B*, 50:16861–16871.

Sottile, F. and Reining, L. (2021a). The kohn-sham potential: Auxiliary system. `https://www.coursera.org/learn/density-functional-theory/lecture/6A6Ge/auxiliary-system-2-3-part1`.

Sottile, F. and Reining, L. (2021b). The many-body wavefunction: a big beast. https://www.coursera.org/learn/density-functional-theory/exam/TEUgp/the-many-body-wavefunction-a-big-beast.

Suzuki, K. Z., Miura, Y., Ranjbar, R., Bainsla, L., Ono, A., Sasaki, Y., and Mizukami, S. (2018). Perpendicular magnetic tunnel junctions with mn-modified ultrathin mnga layer. *Applied Physics Letters*, 112(6):062402.

Tersoff, J. and Hamann, D. R. (1985). Theory of the scanning tunneling microscope. *Phys. Rev. B*, 31:805–813.

Tillard, M. and Belin, C. (2012). Investigation in the ga-rich side of the mn–ga system: Synthesis and crystal structure of mnga4 and mnga5−x (x $\sim$ 0.15). *Intermetallics*, 29:147–154.

Toyir, J., de la Piscina, P. R., Fierro, J. L. G., and Homs, N. (2001a). Catalytic performance for co2 conversion to methanol of gallium-promoted copper-based catalysts: influence of metallic precursors. *Applied Catalysis B: Environmental*, 34(4):255–266.

Toyir, J., de la Piscina, P. R., Fierro, J. L. G., and Homs, N. (2001b). Highly effective conversion of co2 to methanol over supported and promoted copper-based catalysts: influence of support and promoter. *Applied Catalysis B: Environmental*, 29(3):207–215.

Toyir, J., de la Piscina, P. R., Llorca, J., Fierro, J.-L. G., and Homs, N. (2001c). Methanol synthesis from co2 and h2 over gallium promoted copper-based supported catalysts. effect of hydrocarbon impurities in the co2/h2 source. *Physical Chemistry Chemical Physics*, 3(21):4837–4842.

Tran, R., Xu, Z., Radhakrishnan, B., Winston, D., Sun, W., Persson, K. A., and Ong, S. P. (2016). Surface energies of elemental crystals. *Scientific Data*, 3(1):160080.

Vanderbilt, D. (1990). Soft self-consistent pseudopotentials in a generalized eigenvalue formalism. *Phys. Rev. B*, 41:7892–7895.

Wachtel, E. and Nier, K. J. (1965). Magnetische untersuchung des systems mangan-gallium im festen und flüssigen zustand. *International Journal of Materials Research*, 56(11):779–789.

Wang, K., Chinchore, A., Lin, W., Ingram, D. C., Smith, A. R., Hauser, A. J., and Yang, F. (2009). Epitaxial growth of ferromagnetic -phase manganese gallium on semiconducting scandium nitride (001). *Journal of Crystal Growth*, 311(8):2265–2268.

Wei, J. Z., Wu, R., Yang, Y. B., Chen, X. G., Xia, Y. H., Yang, Y. C., Wang, C. S., and Yang, J. B. (2014). Structural properties and large coercivity of bulk mn 3− x ga ($0 \leq x \leq 1.15$). *Journal of Applied Physics*, 115(17):17A736.

Weisstein, Eric W. (2022). Functional. https://mathworld.wolfram.com/Functional.html.

Wirth, M. (2013). The magic of manganese dioxide: What it is and why you should care. https://wcponline.com/2013/03/03/magic-manganese-dioxide-care/.

Wulfhekel, W. and Gao, C. L. (2010). Investigation of non-collinear spin states with scanning tunneling microscopy. *Journal of Physics: Condensed Matter*, 22(8):084021.

Xu, Z., Ao, Z., Yang, M., and Wang, S. (2022). Recent progress in single-atom alloys: Synthesis, properties, and applications in environmental catalysis. *Journal of Hazardous Materials*, 424:127427.

Xue-Shan, L., Jing-Kui, L., and Zhong-Ruo, Y. (1979). The crystal structure of mnga and the degree of order. *Acta Physica Sinica*, 28:54.

Yamada, T., Kunitomi, N., Nakai, Y., E. Cox, D., and Shirane, G. (1970). Magnetic structure of -mn. *Journal of the Physical Society of Japan*, 28(3):615–627.

Yamagata, H. and Asayama, K. (1972). Nmr study of antiferromagnetic -mn metal. *Journal of the Physical Society of Japan*, 33(2):400–408.

Yang, Z., Li, J., sheng Wang, D., Zhang, K., and Xie, X. (1998). Electronic structure and magnetic properties of -mnga. *Journal of Magnetism and Magnetic Materials*, 182(3):369–374.

Yuasa, S., Fukushima, A., Yakushiji, K., Nozaki, T., Konoto, M., Maehara, H., Kubota, H., Taniguchi, T., Arai, H., Imamura, H., Ando, K., Shiota, Y., Bonell, F., Suzuki, Y., Shimomura, N., Kitagawa, E., Ito, J., Fujita, S., Abe, K., Nomura, K., Noguchi, H., and Yoda, H. (2013). Future prospects of mram technologies. pages 3.1.1–3.1.4.

Zha, C. L., Dumas, R. K., Lau, J. W., Mohseni, S. M., Sani, S. R., Golosovsky, I. V., Monsen, A. F., Nogués, J., and Åkerman, J. (2011). Nanostructured mnga films on si/sio2 with 20.5 koe room temperature coercivity. *Journal of Applied Physics*, 110(9):093902.

Zhang, F., Tong, J., Wu, Y., Liu, G., Zhang, R., Tian, F., Qin, G., and Zhang, X. (2021). Interfacial magnetic coupling and orbital hybridization for d0 22 -mn 3 ga/fe films. *Physica Scripta*, 96(7):075804.

Zhang, W. and Cheng, C. Y. (2007). Manganese metallurgy review. part i: Leaching of ores/secondary materials and recovery of electrolytic/chemical manganese dioxide. *Hydrometallurgy*, 89(3–4):137–159.

Zhu, L., Nie, S., Meng, K., Pan, D., Zhao, J., and Zheng, H. (2012). Multifunctional l10-mn1.5ga films with ultrahigh coercivity, giant perpendicular magnetocrystalline anisotropy and large magnetic energy product. *Advanced Materials*, 24(33):4547–4551.

Zhu, L. J., Pan, D., Nie, S. H., Lu, J., and Zhao, J. H. (2013). Tailoring magnetism of multifunctional mnxga films with giant perpendicular anisotropy. *Applied Physics Letters*, 102(13):132403.

Åkerman, J. (2005). Toward a universal memory. *Science*, 308(5721):508–510.

Annex

Annex 1. Surface Formation Energy Formalism

As explained in **Chapter 2** the total energies outputted by DFT calculations depend on the electron density, which also depends (among other things) on the number of electrons in the system. Therefore the energies of systems with different numbers of atoms are not comparable. Therefore, another criterion is needed to compare the stabilities of surface reconstructions with different numbers of atoms and different elements. This tool is the Surface Formation Energy (SFE) formalism, which was firstly described by Qian et al. (1988) and has been applied on several articles ever since (Corbett et al., 2017; Ruvalcaba et al., 2021). Applying this formalism to the present systems goes as follows: first, we must consider that the whole supercell is in thermodynamical equilibrium. Under this consideration, any change in the energy will be given by a change in the number of atoms in the system, *i.e.* their corresponding chemical potentials. Considering any system with less than three elements, such as a Mn-Ga alloy, the previous statement can be mathematically expressed as:

$$E_b = A\sigma + n_{Mn}\mu_{Mn} + n_{Ga}\mu_{Ga} \tag{A.1}$$

where E_b is the total energy of the supercell, A is the cross-sectional area of the surface, σ is the SFE, n is the number of atoms in the unit cell (in α-Mn $n_{Ga} = 0$) and μ is the chemical potential. The subscripts represent the elements to which each parameter is associated. If the SFE of the previous equation is cleared, we obtain:

$$\sigma = \frac{E_b - n_{Mn}\mu_{Mn} - n_{Ga}\mu_{Ga}}{A} \tag{A.2}$$

The enthalpies of formation of the bulk (μ_{bk}) and the surface reconstructions (ΔH_f) are defined as follows:

$$\mu_{bk} = x_{Mn}\mu_{Mn} + x_{Ga}\mu_{Ga} \tag{A.3}$$

$$\Delta H_f = \mu_{bk} - x_{Mn}\mu_{Mn}^{bk} - x_{Ga}\mu_{Ga}^{bk} \tag{A.4}$$

where x represents the number of atoms of each element in the general formula of the alloy: in α-Mn $x_{Mn}, x_{Ga} = 1, 0$, in $D0_{22}$-Mn_3Ga $x_{Mn}, x_{Ga} = 3, 1$, and in $L1_0$-MnGa $x_{Mn}, x_{Ga} = 1, 1$. In addition, μ_{bk}, μ_{Mn}^{bk} and μ_{Ga}^{bk} are the final energies of the alloys, the Mn and the Ga bulks outputted by the calculation. μ_{Mn}^{bk} and μ_{Ga}^{bk} are equal to $-9.01\ eV/atom$ and $-2.91\ eV/atom$, respectively. They were obtained following the same methodology described in **Section 3.2**. The crystal structure of Mn is the α-Mn, and the crystal structure of Ga was taken from Materials Project (2013c). According to its definition,

the enthalpy of formation $\Delta\mu$ is negative when the alloy is more stable than the separate metals and positive when it is less stable. Next, another auxiliary parameter $\Delta\mu$ is defined as:

$$\Delta\mu = x_{Mn}\mu_{Mn} - x_{Ga}\mu_{Ga} \tag{A.5}$$

By solving the system of equations generated by (A.3) and (A.5) we find that:

$$\mu_{Mn} = \frac{\mu_{bk} + \Delta\mu}{2x_{Mn}} \tag{A.6}$$

$$\mu_{Ga} = \frac{\mu_{bk} - \Delta\mu}{2x_{Ga}} \tag{A.7}$$

Then, by substituting equations (A.6) and (A.7) in (A.2) and grouping similar terms we obtain:

$$\sigma = \frac{1}{2A}\left[2E_b - \mu_{bk}\left(\frac{n_{Mn}}{x_{Mn}} + \frac{n_{Ga}}{x_{Ga}}\right) - \Delta\mu\left(\frac{n_{Mn}}{x_{Mn}} - \frac{n_{Ga}}{x_{Ga}}\right)\right] \tag{A.8}$$

All the values in equation (A.9) are known, except for $\Delta\mu$. We are not interested in the region in which the Mn bulk is formed $\left(\mu_{Mn} < \mu_{Mn}^{bk}\right)$ and the same goes for the Ga $\left(\mu_{Ga} < \mu_{Ga}^{bk}\right)$. Therefore the domain of $\Delta\mu$ is defined as:

$$x_{Mn}\mu_{Mn}^{bk} - x_{Ga}\mu_{Ga}^{bk} - \Delta H_f < \Delta\mu < x_{Mn}\mu_{Mn}^{bk} - x_{Ga}\mu_{Ga}^{bk} + \Delta H_f \tag{A.9}$$

According to equation A.5, when the chemical potential of Ga dominates, the last two terms on the left have a negative sign, and $\Delta\mu$ reaches its minimum value at the lower limit. This is referred to as Ga-rich conditions. On the contrary, Mn-rich conditions are met when the chemical potential of Mn dominates, reaching its maximum value at the upper limit. Finally, in **Figures 10(b),14(b)** is plotted the SFE — defined in equation (A.8) — vs $\Delta\mu$ for every proposed surface reconstruction of $D0_{22}$-Mn_3Ga and $L1_0$-MnGa.

In the case of α-Mn, since there is no Ga in the structure, all terms related to Ga in equation (A.8) become zero, and $\Delta\mu$ is only plotted in one point: μ_{bk}. After performing these simplifications, we get the expression for the SFE plotted in **Figure 7(b)**:

$$\sigma_{\alpha\text{-}Mn} = \frac{1}{A}\left(E_b - n_{Mn}\mu_{Mn}^{bk}\right) \tag{A.10}$$

Annex 2. Analyzed surface reconstructions

This section shows the least-stable surface models of all three Mn-Ga alloys.

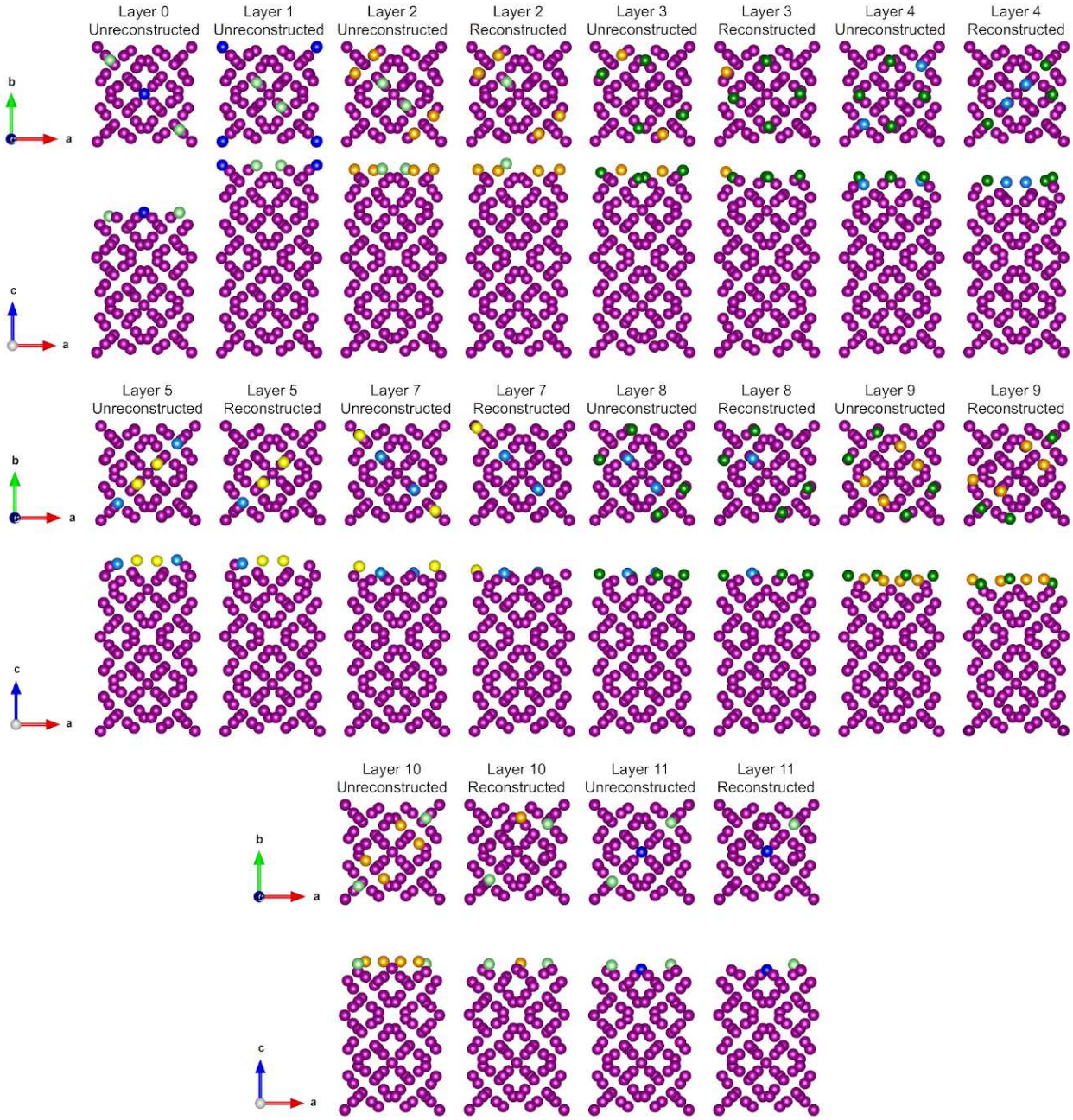

Figure 19. Top and front views of the α-Mn models analyzed with the SFE formalism. See nomenclature in **Section 3.3.1**.

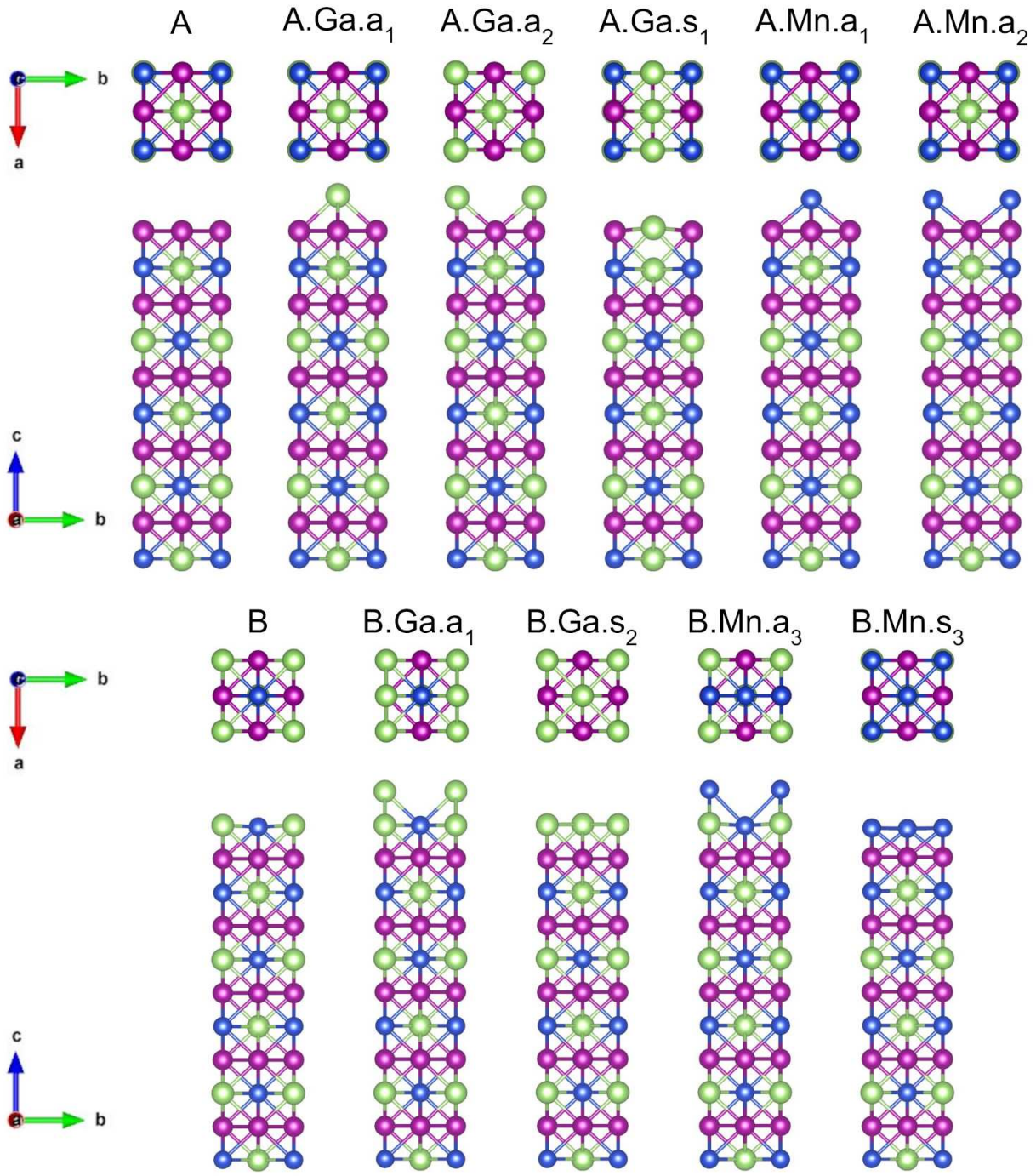

Figure 20. Top and front views of the $D0_{22}$-Mn_3Ga models analyzed with the SFE formalism. See nomenclature in **Section 3.3.2**.

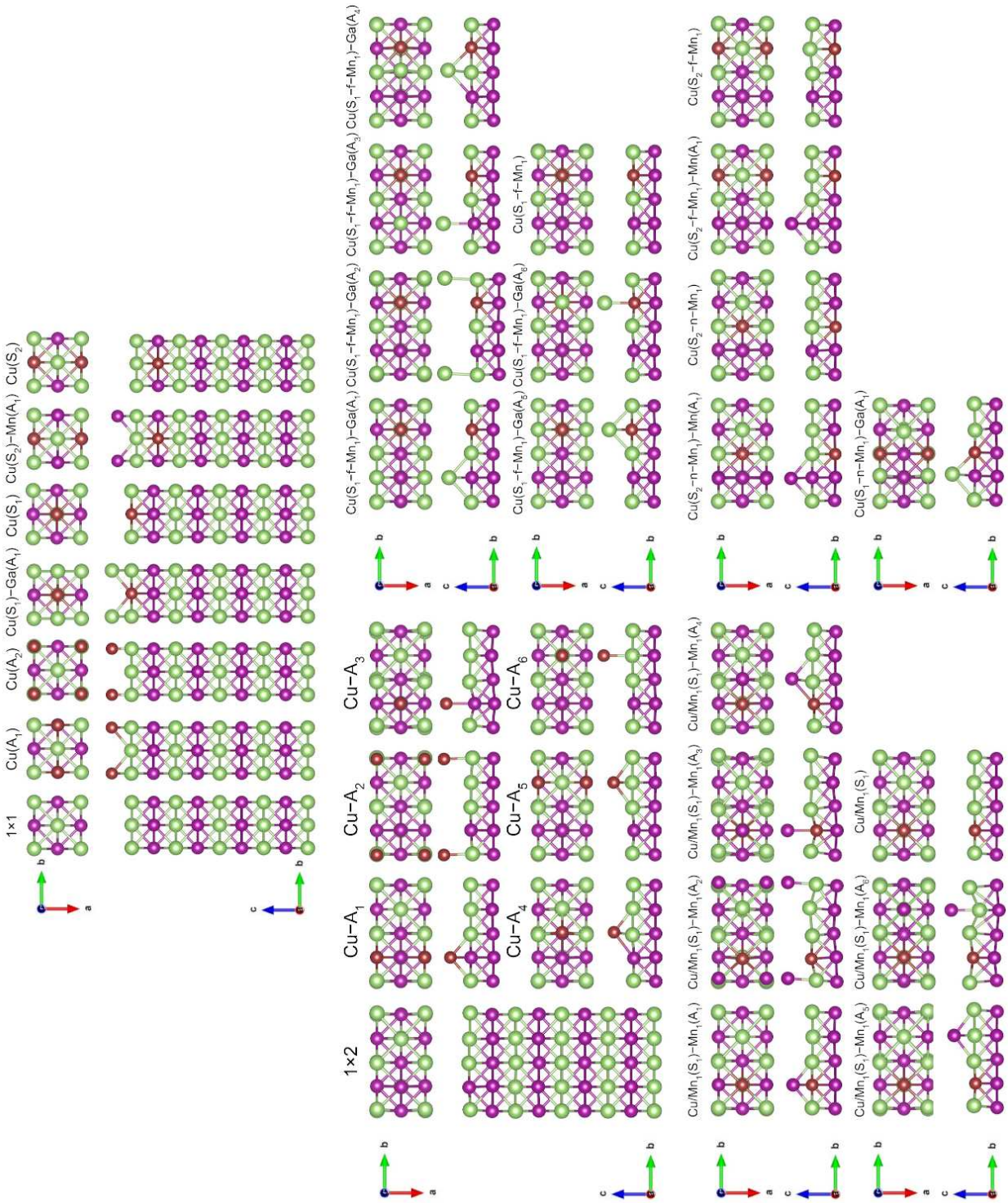

Figure 21. Top and front views of the $L1_0$-MnGa models analyzed with the SFE formalism. Brown spheres represent Cu atoms. S_1 and S_2 stand for substitution of the respective atoms in the first or second layers, respectively. "A" stands for adsorption according to **Figure 6** Letters "f" and "n" stand for "far from" or "near from" the first layer Mn atom, respectively. On the 1×2 reconstructions only the surface-most two layers are shown.